# Effective dispersion in the focusing nonlinear Schrödinger equation

Katelyn Plaisier Leisman,[1] Douglas Zhou,[2] J. W. Banks,[3] Gregor Kovačič,[3] and David Cai[2,4]
[1]*Department of Mathematics, University of Illinois, Urbana, Illinois 61801, USA*
[2]*School of Mathematical Sciences, MOE-LSC, and Institute of Natural Sciences, Shanghai Jiao Tong University, Shanghai 200240, People's Republic of China*
[3]*Rensselaer Polytechnic Institute, Department of Mathematical Sciences, Troy, New York 12180, USA*
[4]*Courant Institute of Mathematical Sciences, New York University, New York, New York 10012, USA*

(Received 1 May 2019; published 19 August 2019)

For waves described by the focusing nonlinear Schrödinger equation (FNLS), we present an effective dispersion relation (EDR) that arises dynamically from the interplay between the linear dispersion and the nonlinearity. The form of this EDR is parabolic for a robust family of "generic" FNLS waves and equals the linear dispersion relation less twice the total wave action of the wave in question multiplied by the square of the nonlinearity parameter. We derive an approximate form of this EDR explicitly in the limit of small nonlinearity and confirm it using the wave-number-frequency spectral (WFS) analysis, a Fourier-transform based method used for determining dispersion relations of observed waves. We also show that it extends to the FNLS the universal EDR formula for the defocusing Majda-McLaughlin-Tabak (MMT) model of weak turbulence. In addition, unexpectedly, even for some spatially periodic versions of multisolitonlike waves, the EDR is still a downward shifted linear-dispersion parabola, but the shift does not have a clear relation to the total wave action. Using WFS analysis and heuristic derivations, we present examples of parabolic and nonparabolic EDRs for FNLS waves and also waves for which no EDR exists.

DOI: 10.1103/PhysRevE.100.022215

## I. INTRODUCTION

The dynamics of many wavelike systems, even those with weak nonlinearities, tend to be turbulent and chaotic [1]. However, when the nonlinearity vanishes, the limiting dynamics become regular and controlled by the system's *linear dispersion relation*. This relation singles out a particular temporal frequency (or a small set of them) corresponding to each spatial wavelength or, equivalently, the phase velocity with which waves with that particular wavelength travel [2]. When a system's nonlinearity is weak, it is not much of a surprise that its linear dispersion relation still features prominently in its dynamics; after all, such a system comprises a collection of weakly coupled plane waves whose dynamics are governed by this relation on short timescales and only modulate slowly in response to the weak nonlinear coupling. There is no reason, however, that a similar scenario should persist into the regime of higher nonlinearities. Yet, in some cases, it does persist in a statistical sense, provided we broaden our concept of dispersion relation [3–6].

Nonlinear interaction of modes is known to give rise to a nonlinear frequency shift [1]: rather than being governed by the linear dispersion relation, the dynamics of a mode with a particular wavelength (or wave number) at least approximately oscillate with an *effective frequency*, which depends on this mode's amplitude. A description of this phenomenon at moderate to strong nonlinearities was provided in Refs. [3,4]. In these works, a *renormalized, effective dispersion relation* (EDR) for the $\beta$-Fermi-Pasta-Ulam (FPU) chain and its corresponding *renormalized Hamiltonian* were established (see also [7,8]). In [5], these concepts were extended to the one-dimensional defocusing Majda-McLaughlin-Tabak (MMT) model of wave turbulence [9–11]. In both cases, despite the relatively strong nonlinearity, the respective system was found to behave statistically as a weakly coupled collection of linear plane waves, with the dynamical evolution of each of these waves dominated by a frequency that depended on its wave number as described by the corresponding EDR. In [5], the form of the EDR was predicted for long waves using the Zwanzig-Mori projection formalism, and confirmed for all wavelengths using the *wave-number-frequency spectral* (WFS) analysis. This analysis is a Fourier-transform based method used to extract dispersion relations from satellite images of oceanic and atmospheric waves [12–15]. Furthermore, EDRs were found using the same techniques for two systems that include no linear dispersion at all: the double-well FPU chain and the fully nonlinear MMT model [6].

In this paper, we study effective dispersion in a specific case of the *focusing* MMT model, namely, the focusing nonlinear Schrödinger equation (FNLS),

$$iq_t = q_{xx} + \alpha^2|q|^2q. \tag{1}$$

In addition to being a ubiquitous model of important nonlinear natural phenomena [16–22], the nonlinear Schrödinger equation stands out from the MMT family because it is completely integrable and thus has an infinite number of conserved quantities [23] (see Appendix A). This contrasts with the general MMT model which only has three [9]. Because the infinity of conserved quantities strongly restricts the FNLS dynamics, and also because of the presence of the highly coherent soliton waves, one might expect that, even in their most general features, the FNLS dynamics may deviate from those of the more general MMT-model cases. Nevertheless,

 

for the FNLS, as well, we find that a robust family of its waves obeys the rather universal EDR form directly extended from the defocusing MMT model [5], and derived in a mathematically rigorous manner for both the focusing and defocusing nonlinear Schrödinger equations in a limit of small amplitudes of the modes [24]. We also find, however, that other FNLS wave families obey different forms of EDRs, or none at all.

We investigate effective dispersion in a robust family of FNLS waves on a periodic domain using three different approaches. First, we exploit the modulational instability of the FNLS plane and standing waves [25–27]. Under perturbation, this instability is known to saturate into waves comprising large collections of nonlinearly interacting modes. Second, we evolve a spatial "white-noise" initial condition. Finally, we use a set of overlapping solitonlike, sech-shaped waves as a yet different initial condition. In all three cases, the resulting waves are governed by the EDR extended from that of the defocusing MMT model [5] and of the nonlinear Schrödinger equation in the limit of small amplitudes of the modes [24]: the quadratic linear dispersion relation, displaced downward by twice the product of the total wave action of this wave and the square of the nonlinearity parameter $\alpha$. We compute this EDR numerically using WFS analysis, and also derive it in the limit of small nonlinearity.

The integrable structure of the FNLS gives us easy access to coherent structures such as solitons. It is not clear that waves containing such structures can have associated EDRs, and, in fact, we find evidence that some do and some do not. The EDR of a soliton can be derived in closed form, and is represented by a straight line; WFS analysis confirms that this EDR remains largely undisturbed for spatially periodic FNLS waves with solitonlike initial conditions. Surprisingly, for spatially periodic versions of well-separated multisolitons with equal amplitudes, the EDR is again parabolic. However, we find its downward shift from the linear dispersion relation to differ from that expected from the case of the robust wave family discussed in the previous paragraph. There also exist, of course, FNLS waves with no effective dispersion relation, such as the multi-breather-like waves emerging from specific sech-like initial conditions [28], as the dynamics of the modes composing these waves simply do not behave sinusoidally. In other words, these waves are not families of weakly coupled plane waves. Finally, we also find combinations of dispersive waves with coherent structures, which again lack clearly defined EDRs.

The remainder of this paper is organized as follows: In Sec. II, we introduce the idea of an EDR, first describing it as a nonlinear analog to the dispersion relation for autonomous linear wave systems in Sec. II A, and then describing how to measure it using WFS analysis in Sec. II B. In Sec. III, we discuss the EDRs, or the absence of an EDR, for a number of different families of FNLS waves. In particular, in Sec. III A, we explicitly derive the EDR in the case of weak nonlinearity and confirm it for a robust family of waves generated either from the saturation of weakly perturbed, modulationally unstable plane waves or from noiselike spatial initial conditions. In Sec. III B, we find some EDRs for waves that comprise or contain coherent structures on a spatially periodic interval, such as a single "soliton"-like wave and well-separated, equidistant periodic "multisoliton"-like waves. We also display waves that possess no EDR, and waves containing coherent structures for which the EDRs have unusual or ambiguous shapes. We present conclusions in Sec. IV. In Appendix A, we briefly outline the inverse scattering transform used to find exact solutions of the FNLS equation. In Appendix B, we give details of the EDR derivation for weak nonlinearity. In Appendix C we outline the limit of small amplitudes of the modes. In Appendix D, we review the modulational instability of plane waves. In Appendix E, we describe how we generate two types of random initial conditions for FNLS waves. In Appendix F, we outline the WFS analysis of the single soliton.

## II. EFFECTIVE DISPERSION RELATION

In this section, we describe the concept of an EDR, as well as a method used to measure it in an observation or a numerical simulation.

### A. Effective dispersion relation as a nonlinear analog of linear dispersion relation

The dispersion relation in an autonomous linear wave system relates the spatial wave number $k$ and the temporal frequency $\omega$ of the plane-wave modes, $e^{-i(kx-\omega t)}$, that compose the dynamical states of such a system via linear superposition. For example, for the linear Schrödinger equation describing a free particle, $iq_t = q_{xx}$, substituting $q \sim e^{-i(kx-\omega t)}$ yields the dispersion relation $\omega = k^2$. In this case, since $\omega(k)$ is real-valued for $k$ real, the modes evolve as harmonic waves. Since $\omega''(k) \not\equiv 0$, the evolution of these waves is dispersive in the sense that different plane waves travel with different velocities. The corresponding group velocity of wave packets centered at the wave number $k$ is $V_g = \omega'(k) = 2k$ [2].

Since nonlinear waves generally need not evolve as harmonic superpositions of plane waves, the above linear picture does not usually apply to them. Nevertheless, weakly nonlinear waves typically act as collections of weakly coupled plane waves. They evolve approximately according to the dispersion relation of the limiting linear system on short timescales, and their amplitudes are modulated by the coupling via the nonlinearity on long timescales, inversely related to the size of the nonlinearity.

For highly nonlinear wave systems (such as the FNLS when the nonlinearity parameter $\alpha$ is large), even the above weakly nonlinear scenario is implausible. Therefore, in this case, one must be careful when discussing the possibility of a dispersion relation at all: Although we can still decompose nonlinear waves into spatial Fourier modes at any given moment in time, these modes will not necessarily evolve periodically in time with any particular frequency, nor will their dynamics only be weakly coupled. Nevertheless, in a statistical steady state, certain nonlinear wave systems do generate dynamics that appear to behave effectively over long timescales as weakly coupled collections of linear plane waves, and our work suggests that the FNLS is one of these systems. Of course, the linear dispersion relations of their limiting weakly nonlinear systems cannot be expected to capture these dynamics correctly. Instead, for each special nonlinear wave in such a system, we need to consider a possible EDR

that includes the contribution of the nonlinearity as well. Moreover, one cannot expect that any plane-wave modes will evolve periodically in time even in a system for which an EDR exists; such a periodic evolution only manifests itself statistically, on very long timescales, as a dominant temporal frequency of a given mode's dynamics. A definition of the EDR which also serves as a way of measuring it in any wave system is given next.

### B. Measuring effective dispersion relation

Since we are looking for a relation between the spatial wave numbers and the temporal frequencies, it makes sense to study the Fourier transform of the wave under investigation in both space and time. For linear waves, this would lead directly to the dispersion relation. For nonlinear waves, there need not exist a dominant temporal frequency $\omega = \omega(k)$ for a given wave number $k$ even in a statistical steady state.

The *wave-number-frequency spectral* (WFS) analysis, an experimental method typically used to extract dispersion relations from measured images of water or atmospheric waves [12–15], can be used to investigate both the existence and shape of EDRs. This method finds the peak frequency $\omega$ of the power spectral density (PSD) for each wave number $k$:

$$\omega(k) = \arg\max_{\omega} \lim_{T\to\infty} \frac{1}{T}\left|\int_0^T \hat{q}(k,t)e^{-i\omega t}\,dt\right|^2, \tag{2}$$

if such a peak exists, where

$$\hat{q}(k,t) = \int_{-\infty}^{\infty} q(x,t)e^{-ikx}\,dx \tag{3}$$

is the spatial Fourier Transform of the wave $q(x,t)$. We will use this method to compute the EDRs of all the waves simulated numerically in this paper.

We remark that, in practice, the limit in Eq. (2) is approximated by averaging over a sequence of finite-duration time windows, $(j-1)T_{\text{win}} < t < jT_{\text{win}}$, with $j = 1,\ldots,J$, and some appropriately chosen window length $T_{\text{win}}$. The formula in Eq. (2) is thus replaced by the approximate equation

$$\omega(k) \approx \arg\max_{\omega} \frac{1}{JT_{\text{win}}} \sum_{j=1}^{J}\left|\int_{(j-1)T_{\text{win}}}^{jT_{\text{win}}} \hat{q}(k,t)e^{-i\omega t}\,dt\right|^2. \tag{4}$$

This approximation can be justified by the fact that the right-hand-side of the FNLS in Eq. (1) contains no explicit time dependence and by the ergodic hypothesis, and is employed to improve the signal-to-noise ratio [29].

## III. EFFECTIVE DISPERSION RELATIONS FOR WAVES OF THE FOCUSING NONLINEAR SCHRÖDINGER EQUATION

In this section, we present several EDRs for FNLS waves on a periodic domain, so that the periodic boundary condition,

$$q(x+L,t) = q(x,t), \tag{5}$$

holds for a fixed period $L$ and for any solution $q(x,t)$ of the FNLS model in Eq. (1). We derive EDRs for small nonlinearities, and confirm their validity for a robust family of numerically simulated waves using WFS analysis. We also derive EDRs for periodic versions of solitons and some multi-solitons, and display some waves for which no unambiguous EDRs appear to exist.

We simulated FNLS waves numerically using both a Fourier split-step method [26], which is first-order accurate in $t$ and accurate to machine error in $x$ [30], and a pseudospectral approach using Fourier transforms to evaluate spatial derivatives [31] along with classical fourth-order Runge-Kutta time stepping [32]. The results of these two methods were indistinguishable for the results of this paper, so the figures included here were obtained by the split-step method. In all the figure captions to follow, we denote the total number of spatial discretization intervals by $N_x$, their length by $\Delta x$ $(= L/N_x)$, and the time step by $\Delta t$.

### A. Effective dispersion relation for a robust family of waves

In this section, we derive an approximate EDR for FNLS waves in the limit of small nonlinearity, and extend its validity to arbitrary nonlinearity values within a robust wave family.

#### *1. Effective dispersion relation for weak nonlinearities*

For illustration, we first derive an approximate EDR for weakly nonlinear FNLS waves, i.e., for the case when the nonlinearity parameter $\alpha$ in Eq. (1) is small. In the next section, we show numerically that it holds for a robust class of waves with arbitrary values of $\alpha$ as well.

For $\alpha \ll 1$, an FNLS wave can be expanded as

$$\begin{aligned} q(x,t) &= \sum_{n=-\infty}^{\infty} a_{k_n}(t)e^{-ik_n x} \\ &= \sum_{n=-\infty}^{\infty} a_{k_n}(0) \\ &\quad \times e^{-i\{k_n x - [k_n^2 - \alpha^2(2\|a_\kappa(0)\|_2^2 - |a_{k_n}(0)|^2)]t\}} + O(\alpha^2), \end{aligned} \tag{6}$$

where $k_n = 2\pi n/L$ is the wave number and

$$\|a_\kappa(0)\|_2^2 = \|a_\kappa(t)\|_2^2 \equiv \sum_{m=-\infty}^{\infty} |a_{k_m}(0)|^2 = \sum_{m=-\infty}^{\infty} |a_{k_m}(t)|^2 \tag{7}$$

is the conserved total wave action. (For a derivation, see Appendix B.) The expansion in Eq. (6) is valid on timescales of $O(\alpha^{-2})$, and shows that the mode with the wave number $k_n$ evolves in time with the effective frequency

$$\omega(k_n) \approx k_n^2 - \alpha^2\left(2\|a_\kappa(0)\|_2^2 - |a_{k_n}(0)|^2\right). \tag{8}$$

Note that the mode amplitudes $|a_{k_n}(0)|$ are conserved on $O(\alpha^{-2})$ timescales for small values of the nonlinearity parameter $\alpha$, which is not the case for moderate or large $\alpha$. (For a comment on this fact, see Appendix B.)

If all the mode amplitudes in the EDR in Eq. (8) are small compared to the total wave action, then this approximate EDR reduces to

$$\omega(k) \approx k^2 - 2\alpha^2\|a_\kappa(0)\|_2^2 = k^2 - \frac{2\alpha^2}{L}\int_{-L/2}^{L/2} |q(x,0)|^2 dx, \tag{9}$$

where

$$\frac{1}{L}\int_{-L/2}^{L/2}|q(x,0)|^2dx \equiv \frac{1}{L}\|q(x,0)\|_2^2$$

equals the second moment of the wave profile $q(x,0)$, and $\|q(x,0)\|_2^2$ is the squared $L_2$ norm of this profile. Because the total wave action $\|a_\kappa(t)\|_2^2 = (1/L)\|q(x,t)\|_2^2$ is conserved in time, the initial time $t=0$ can be replaced by arbitrary time $t$ in the EDR in Eq. (9).

We remark that the EDR in Eq. (9) is the FNLS analog of the EDR expression derived in Ref. [5] for the general defocusing MMT model using the Zwanzig-Mori [33] theory. This latter derivation is valid for long waves, i.e., small wave numbers $k$. The same EDR expression was also derived in a mathematically rigorous fashion for waves of both the focusing and defocusing nonlinear Schrödinger equations in the limit of small amplitudes of the modes [24], which, after some transforming, can be seen to include the limit of weak nonlinearity discussed here. Details of the relation between the two limits are presented in Appendix C.

As we will see next, numerical simulations strongly indicate that the EDR in Eq. (9) in fact holds for all values of the nonlinearity in a robust class of FNLS waves.

#### 2. *Effective dispersion relation for moderate and large nonlinearities*

We sample a robust family of FNLS waves in two different ways. First, we exploit the modulational-instability saturation of the FNLS plane and standing waves. Second, we evolve spatial-white-noise-like initial conditions. Using the WFS analysis, we numerically compute the EDRs of the resulting waves. We comment on the robustness of this family at the end of this section.

A plane wave,

$$q(x,t) = Ae^{-i[\gamma x-(\gamma^2-A^2\alpha^2)t]}, \tag{10}$$

is an exact solution of the FNLS model in Eq. (1), which exhibits modulational instability [25–27], as discussed in Appendix D. A special case is the standing wave when $\gamma = 0$. As mentioned above, perturbations of the plane waves in Eq. (10) give rise to a robust class of spatiotemporally disordered solutions, which we will use to confirm the validity of the EDR in Eq. (9) for broad ranges of wave numbers and different values of the nonlinearity parameter $\alpha$.

When an initial plane wave with amplitude $A$ and nonlinearity parameter $\alpha$ is propagated in the spatial interval $|x| < L/2$, the number of modes that will experience exponential growth due to the FNLS modulational instability is $2N+1$, where $N$ is the largest integer such that

$$1 \leqslant N \leqslant \frac{\sqrt{2}|A|\alpha L}{2\pi} \tag{11}$$

(see Appendix D). This growth saturates due to the conservation of the total wave action, typically into a wave disordered in space and time. When $|A|\alpha L$ is large, we use WFS analysis to compute that this wave's EDR is a parabola, which extends throughout the wave-number range of the associated unstable modes. This result is illustrated in Figs. 1 and 2, where both waves were generated from an initial condition of a weakly perturbed standing wave with amplitude $A = 72$ on the spatial domain with $L = 2\pi$. We used the initial condition

$$q_0(x) = A\left(1+\sum_{-N}^{N}\varepsilon_n e^{2\pi i n x/L}\right), \tag{12}$$

where $\varepsilon_n$ are randomly generated from a uniform distribution on the interval $|\varepsilon_n| < 10^{-4}$, and where $N$ is as before and in Eq. (11).

In both Figs. 1 and 2 (and in most other figures), panel (a) depicts the space-time profiles of the wave, panel (b) depicts the wave at $t=0$ (red) and at a later time (blue) in $x$ space and panel (c) the same in $k$ space, panel (d) depicts the PSD dependence on the wave number $k$ and frequency $\omega$, and panel (e) depicts the EDR obtained using WFS analysis by finding the peak-frequency $\omega$ values for each wave number $k$ of the PSD in panel (d). Here, all the peaks of the PSD within a given percentage of the global peak value at every $k$ were marked with a blue dot. The percentage is selected to maximize the signal-to-noise ratio in depicting the EDR, and is listed in each figure caption. The wave in Fig. 1 was computed with nonlinearity parameter $\alpha^2 = 1/16$, leading to about 50 unstable modes, while the wave in Fig. 2 was computed with $\alpha^2 = 256$, leading to about 3200 unstable modes. The dots extending beyond the parabola for large $|k|$ in panel (e) of both plots are numerical artifacts; in these regions no single frequency dominates, but the power is also extremely small [$O(10^{-2})$ compared with $O(10^2)$ around $k=0$]. In principle, according to Eq. (2), increasing the computational time $T$ would yield a smooth parabolic EDR (blue) in panel (e) and eliminate the noise. What is of particular interest here is that in both cases (weak and strong nonlinearity), the WFS analysis produces a parabola—the exact parabola predicted in Eq. (9)—for which our derivation was only valid for small nonlinearity $\alpha$.

An alternative way to find spatially disordered waves is to consider those that initially appear white-noise-like in space. (See Appendix E for details.) Such a wave is illustrated in Fig. 3, where the nonlinearity parameter was $\alpha^2 = 1/16$. The spatiotemporal profile of the wave in Fig. 3 appears similar to its counterparts in Figs. 1 and 2, but the distribution of the mode amplitudes in the wave-number space is significantly broader. In fact, all the modes in the available (periodic) range of wave numbers appear to be excited. Nevertheless, the corresponding EDR is again the parabola predicted in Eq. (9).

We remark that not all the waves discussed in this section are closely related to the waves in the limit of small nonlinearity whose EDR we derived explicitly in Sec III A. In particular, waves in the limit of small nonlinearity, approximated by Eq. (6), cannot grow and do not result from any kind of an instability. If we make the assumption that a linear mode will become unstable at the latest when its amplitude would trigger the modulational instability of equal-size traveling wave in Eq. (10), then we see that for waves approximated by Eq. (6) to exist in the assumed form, the nonlinearity parameter $\alpha$ must satisfy the inequalities

$$\alpha \ll \frac{\sqrt{2}\pi}{L|a_{k_n}(0)|} \tag{13}$$

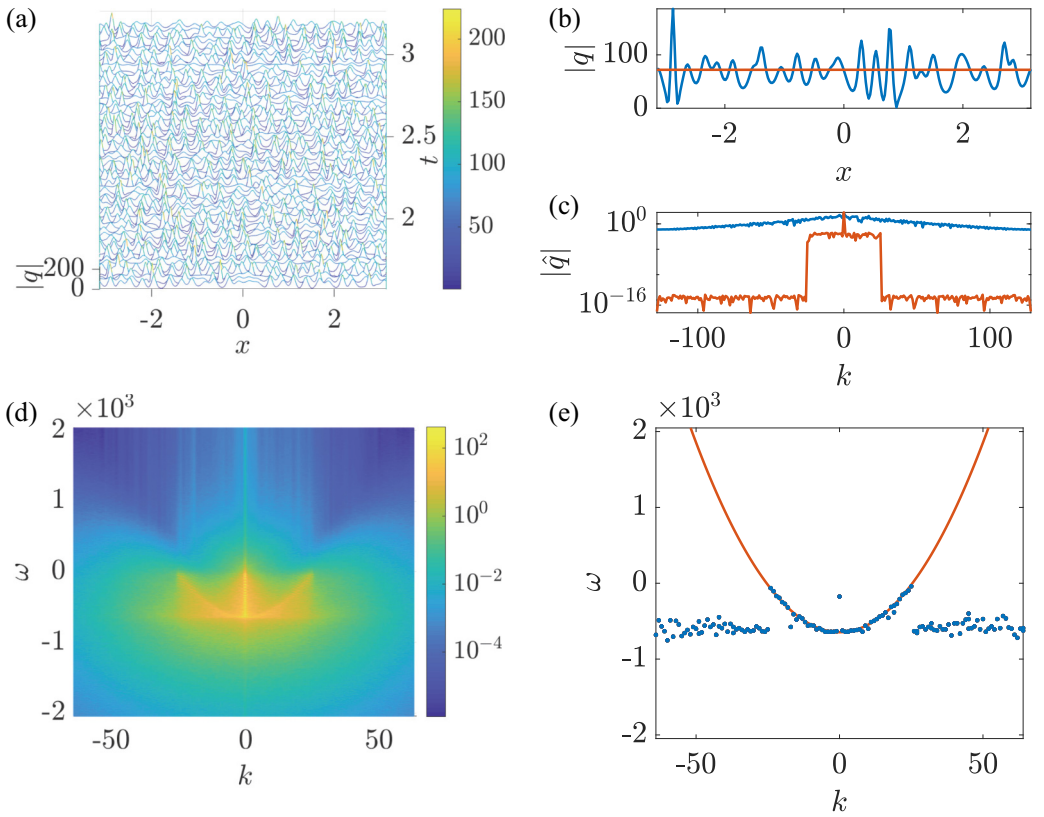


FIG. 1. FNLS wave generated from an initial perturbed standing wave with amplitude $A = 72$, using $\alpha^2 = 1/16$, leading to approximately 50 unstable modes. The computational domain uses $L = 2\pi$ with $N_x = 2^{10}$, $\Delta t = \Delta x^2/2\pi$, and a final time $T = 6\pi$. (a) Three-dimensional space-time profile of the wave at constant-time slices, where color indicates the wave amplitude $|q(x,t)|$. To avoid diagnosing initial transient, the wave is depicted from time $t = \pi/2$ to $t = \pi$. (b) The initial spatial wave profile of a perturbed standing wave in Eq. (12) at $t = 0$ (red), and an example of the evolved wave profile at a $t = \pi$ (blue). (c) The wave-number dependence of the wave's Fourier amplitude, $|\hat{q}(k,t)|$ defined in Eq. (3), in logarithmic scale at $t = 0$ (red) and at $t = \pi$ (blue). According to Eq. (12), the initial wave-number dependence of the wave consists of the standing wave at $k = 0$ and plane-wave perturbations within the $k$-interval of width $\sqrt{2}|A|\alpha$. [cf. Eq. (11)]. Note that the initial random perturbation is masked in the logarithmic scale. (d) The spatiotemporal PSD of the wave, i.e., the argument on the right-hand side of Eq. (2), used in the WFS analysis, plotted with a logarithmic color axis. (e) EDR obtained according to the WFS analysis by finding the peak frequency $\omega$ values for each wave number $k$ of the PSD in panel (d). Here, all the peaks of the PSD within 1% of the global peak value at every $k$ were marked with a blue dot. The resulting EDR (blue) is compared with the theoretically predicted parabolic EDR in Eq. (9) (red). Panels (d) and (e) were computed using the argument in Eq. (4) and employed averaging over 24 windows of width $T_{\text{win}} = \pi/4$.

for all integer $n$, which follow from Eq. (11). Nevertheless, weakly nonlinear waves approximated by Eq. (6) may result from small spatial white-noise-like initial conditions.

We should also remark that the derivation of the EDR in Eq. (9), as carried out in Sec III A, should easily generalize to the defocusing nonlinear Schrödinger model, and even the defocusing MMT model. This is because waves in these models do not experience modulational instability [26], and thus no restrictions on the nonlinearity parameter $\alpha$ of the sort discussed in the previous paragraph are needed. Nevertheless, we should recall that, in all cases, the derivation assumes asymptotically small values of $\alpha$.

We finally remark that the exact solutions of the FNLS with periodic boundary conditions are given in terms of Riemann theta functions associated with Riemann surfaces of arbitrarily high and even infinite genus [34,35]. These solutions can be probed numerically by perturbing plane and standing waves and exploiting the modulational instability [36–39]. In this way, using not necessarily infinitesimal perturbations, it should be possible to access robust solution families of the FNLS with spatially periodic boundary conditions, although any rigorous justification of this claim is far beyond the scope of this paper. We believe the same should hold for spatial white-noise-like initial waves.

### B. Effective dispersion relations for waves containing coherent structures

FNLS waves on the infinite line can be described exactly using the inverse scattering transform, and shown to comprise solitons and radiation [17,18,20,22,23], with the former deemed to be *coherent structures*. Mathematically, solitons correspond to the (time-conserved) discrete eigenvalues of the scattering problem associated with the FNLS and the corresponding norming constants, and the radiation arises from its continuous spectrum and the corresponding reflection coefficient. (Details are reviewed in Appendix A.)

In this section, we consider several (multi)solitonlike FNLS waves, and other FNLS waves containing or comprising coherent structures, on periodic domains. For a

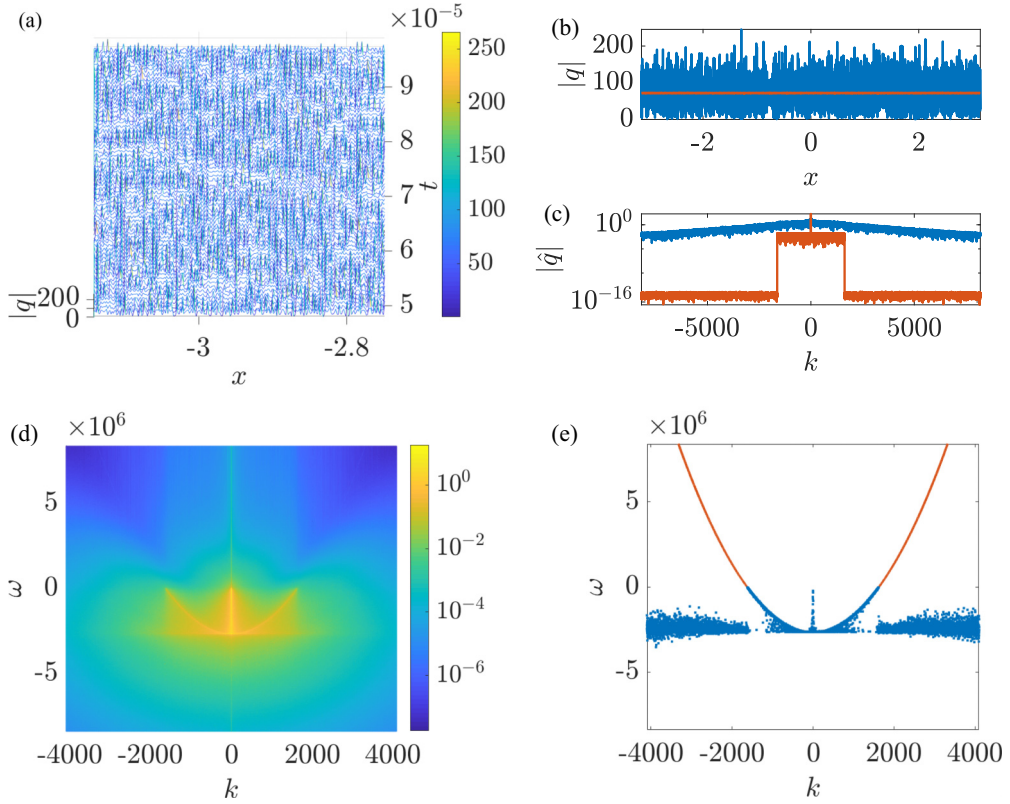


FIG. 2. FNLS wave generated from an initial perturbed standing wave with amplitude $A = 72$, using $\alpha^2 = 256$, leading to approximately 3200 unstable modes. The computational domain uses $L = 2\pi$ with $N_x = 2^{16}$, $\Delta t = \Delta x^2/2\pi$, and a final time $T = 3\pi/2^{11}$. (a) Three-dimensional space-time profile of the wave at constant-time slices, where color indicates the wave amplitude $|q(x,t)|$. To avoid diagnosing initial transient, the wave is depicted from time $t = \pi/2^{16}$ to $t = \pi/2^{15}$. Note that in this figure, the spatial domain has been restricted to $x \in [-\pi, -7\pi/8]$ to more clearly indicate the increased density of wave crests, in comparison with Fig. 1(a). (b) The initial spatial wave profile of a perturbed standing wave in Eq. (12) at $t = 0$ (red), and an example of the evolved wave profile at a $t = \pi/2^{12}$ (blue). (c) The wave-number dependence of the wave's Fourier amplitude $|\hat{q}(k,t)|$, defined in Eq. (3), in logarithmic scale at $t = 0$ (red) and at $t = \pi/2^{12}$ (blue). According to Eq. (12), the initial wave-number dependence of the wave consists of the standing wave at $k = 0$ and plane-wave perturbations within the $k$-interval of width $\sqrt{2}|A|\alpha$. [cf. Eq. (11).] Note that the initial random perturbation is masked in the logarithmic scale. (d) The spatiotemporal PSD of the wave, i.e., the argument on the right-hand side of Eq. (2), used in the WFS analysis, plotted with a logarithmic color axis. (e) EDR obtained according to the WFS analysis by finding the peak frequency $\omega$ values for each wave number $k$ of the PSD in panel (d). Here, all the peaks of the PSD within 1% of the global peak value at every $k$ were marked with a blue dot. The resulting EDR (blue) is compared with the theoretically predicted parabolic EDR in Eq. (9) (red). Panels (d) and (e) were computed using the argument in Eq. (4) and employed averaging over 24 windows of width $T_{\text{win}} = \pi/2^{14}$.

single-soliton-like wave, we find a straight-line EDR. For one multisoliton family, we find an EDR that is again a shifted quadratic parabola. We also display multisolitonlike waves that clearly possess no EDR. Finally, we discuss waves containing coherent structures for which the existence of an EDR is ambiguous.

#### *1. Effective dispersion relation of a single "soliton"*

A single FNLS soliton is described by the formula

$$q(x,t) = \frac{\sqrt{2}A}{\alpha} e^{i[(V^2-A^2)t - Vx + \psi]} \operatorname{sech}\left[A(x - 2Vt - \delta)\right], \tag{14}$$

and corresponds to a single eigenvalue

$$\zeta = \frac{V + iA}{2} \tag{15}$$

of the scattering problem associated with the FNLS, described in Appendix A. Carrying out the WFS method in Eq. (2) explicitly on this soliton by taking both its spatial and temporal Fourier transforms results in the expression for the PSD under the limit in Eq. (2) being equal to

$$\text{PSD}(k) = \frac{2\pi^2}{\alpha^2 T} \operatorname{sech}^2 \frac{\pi(V+k)}{A} \frac{\sin^2[(\Omega(k)+\omega)T/2]}{(\Omega(k)+\omega)^2/4}, \tag{16}$$

where

$$\Omega(k) = A^2 + V^2 + 2Vk. \tag{17}$$

(Details are given in Appendix F.) For a given wave number $k$ and any final time $T$, this expression is clearly the largest when the frequency satisfies the equation $\omega = -\Omega(k)$, which gives the straight-line EDR

$$\omega(k) = -(A^2 + V^2) - 2Vk. \tag{18}$$

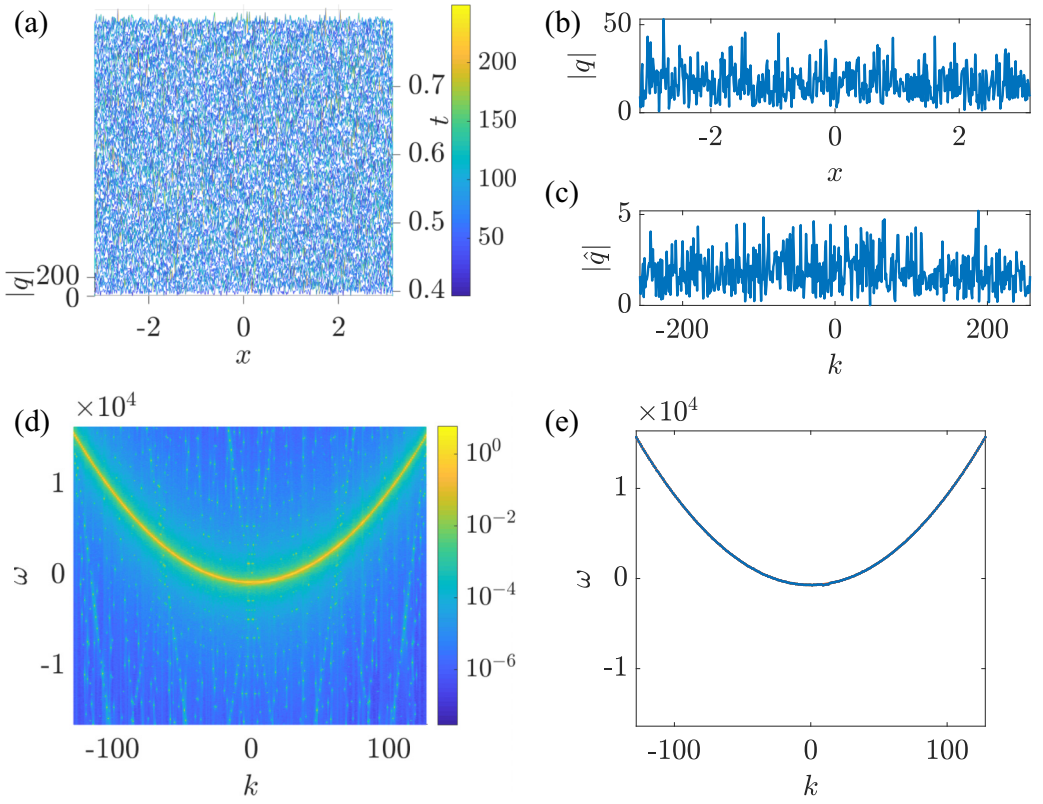


FIG. 3. FNLS wave generated from an initial condition of spatial "white noise." The nonlinearity parameter is $\alpha^2 = 1/16$, the computational domain uses $L = 2\pi$, $N_x = 2^{12}$, $\Delta t = \Delta x^2/2\pi$, and a final time $T = \pi/4$. (a) Three-dimensional space-time profile of the wave at constant-time slices, where color indicates the wave amplitude $|q(x,t)|$. The wave is depicted from time $t = \pi/8$ to $t = \pi/4$. (b) The initial spatial wave profile of "white noise" at $t = 0$, generated as described in Appendix E. (c) The wave-number dependence of the wave's Fourier amplitude $|\hat{q}(k,t)|$, defined in Eq. (3), at $t = 0$. Note that neither the spatial profile or Fourier spectrum of the evolved wave are shown since they appear similar to the initial profile (in contrast to Figs. 1 and 2). (d) The spatiotemporal PSD of the wave, i.e., the argument on the right-hand side of Eq. (2), used in the WFS analysis, plotted with a logarithmic color axis. (e) EDR obtained according to the WFS analysis by finding the peak frequency $\omega$ values for each wave number $k$ of the PSD in panel (d). Here, all the peaks of the PSD within 1% of the global peak value at every $k$ were marked with a blue dot. The theoretically predicted parabolic EDR in Eq. (9) is nearly indistinguishable from the observed EDR for this case. Panels (d) and (e) were computed using the argument in Eq. (4) and employed averaging over 4 windows of width $T_{\text{win}} = \pi/16$.

When we numerically evolve an initial condition of a single-soliton-like wave in Eq. (14), restricted to the spatial interval $-L/2 < x < L/2$, the pulse travels at first like the soliton, until it reaches an end of the spatial interval at $x = L/2$ or $x = -L/2$, and then the numerical solution reappears at the opposite end to continue propagation. This is illustrated in Fig. 4, where $A = 32$, $V = 2$, $\delta = \psi = 0$, and nonlinearity parameter $\alpha = 1$. A fit to the bright line in the results of the WFS method in Eq. (2), displayed Fig. 4(b), indicates the straight-line EDR $\omega(k) = -4k - 1028$, which is exactly the line in Eq. (18) with $A = 32$ and $V = 2$. In Fig. 4(c), the two lines appear to be indistinguishable.

Features that do not directly pertain to the EDR also appear in the spectrum of the numerical solution [Fig. 4(b)]. For example, one can observe faint parabolalike curves in addition to the straight line. All these features repeat periodically in $\omega$, and only a single period is plotted. (The periodicity in $\omega$ is an artifact of the temporal Discrete Fourier Transform.) In this example, when $|k|$ is small, the parabolalike curve approaches the true parabola $\omega = k^2$. However, when $|k|$ is large, this curve approaches the true parabola $\omega = k^2 - 40.63$, which exactly corresponds to Eq. (9): $2\alpha^2\|a_\kappa(0)\|_2^2 = 40.66$. This parabolalike curve in Fig. 4(b) is present because of the boundary effects affecting the "soliton" wave and corresponds to parts of the wave that are radiationlike.

#### 2. *Waves without effective dispersion relation*

Not every FNLS wave has an EDR associated with it. For special amplitude values of a single, stationary, sech-like pulse initial condition, the resulting "breather"-type waves do not have an EDR. For some other multisoliton-type waves, WFS analysis also results in collections of curves that clearly indicate the absence of an EDR.

As one example, alluded to in the preceding paragraph, we look at the FNLS wave satisfying the initial condition

$$q(x,0) = \frac{\sqrt{2}AM}{\alpha}\,\mathrm{sech}(Ax). \tag{19}$$

As shown in Ref. [28], for positive-integer values of the parameter $M$, this wave comprises $M$ solitons and no radiation, with each soliton corresponding to one of the $M$ distinct

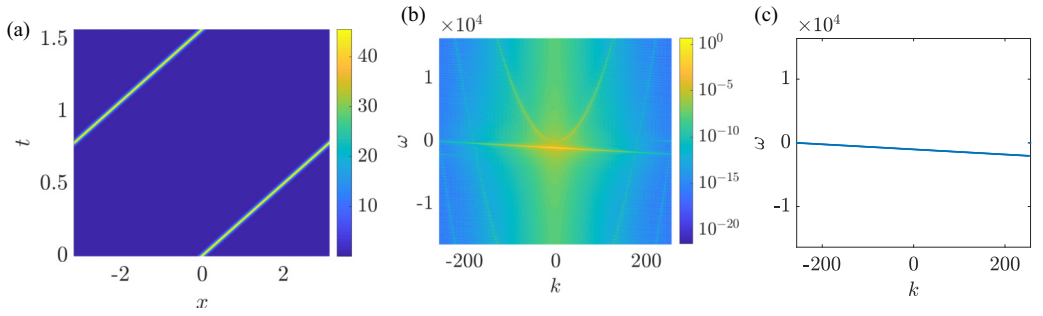


FIG. 4. Single "soliton" wave of Eq. (14), with parameters: $A = 32$, $V = 2$, $\delta = 0$, $\psi = 0$, and $\alpha = 1$. The computational domain was $L = 2\pi$ with $N_x = 2^9$, $\Delta t = \Delta x^2/2\pi$, and final time $T = \pi/2$. (a) Color contour plot of the wave where the color indicates the magnitude of the wave amplitude $|q(x,t)|$. (b) The spatiotemporal PSD of the wave, i.e., the argument on the right-hand side of Eq. (2), used in the WFS analysis, plotted using a logarithmic color scale. (c) EDR obtained according to the WFS analysis by finding the peak frequency $\omega$ values for each wave number $k$ of the PSD in panel (b). Here, all the peaks of the PSD within 1% of the global peak value at every $k$ were marked with a blue dot. A least-square fit line to this data is $\omega = -4k - 1028$, which corresponds to the expected EDR from Eq. (18). Note that the PSD along the faint parabola visible in panel (b) is four orders of magnitude smaller that that along the line near $k = 0$. Panels (b) and (c) were computed using the argument in Eq. (4) over a single time window of length $T_{\text{win}} = T$.

eigenvalues $\zeta_j = iA(j - 1/2)$, $j = 1, 2, \ldots, M$, of the scattering problem associated with the FNLS. This wave is called a multi-"breather," and changes its shape periodically in time but remains centered about the origin [28], as displayed in Fig. 5(a). The fact that this wave remains in the same location can also be gleaned from Eqs. (14) and (15) and the fact that the eigenvalues $\zeta_j$ are pure imaginary, from which one can see that its constituent solitons have vanishing velocities.

For the single soliton in Eq. (14), we could write the EDR in Eq. (18) in terms of the corresponding discrete eigenvalue $\zeta = (V + iA)/2$ in Eq. (15) as $\omega(k) = -|2\zeta|^2 - 2(\zeta + \zeta^*)k$. This form of the EDR would suggest that in the WFS analysis of the $M$-soliton wave emerging from the initial wave in Eq. (19), we might see $M$ horizontal lines corresponding to the frequencies $\omega_j = -[2A(j - 1/2)]^2$. Indeed, when $A = 4$ and $M = 4$, as shown in Fig. 5, we see $\omega = -16, -144, -400, -784$ (though in this case we also see many other multiples of 128 away from $-16$, which may be harmonics). In this case, we cannot find a single-valued function $\omega(k)$ signifying a dominant effective frequency for any given mode in the respective waves. Clearly, these waves are composed of modes whose temporal harmonics appear to be as prominent as their fundamental frequencies, and so they do not undergo time-harmonic motion.

More generally, the computation of even just the initial conditions for exact multisoliton waves becomes increasingly poorly conditioned with the increasing number of solitons [40]. Alternatively, however, if the pulses are sufficiently far apart at $t = 0$, a sum of single-soliton-like pulses provides a reasonable approximation to such an initial wave when propagated numerically in time. Typically, the pulses seem to each contribute a linear piece to the wave-number-dependent PSD, reminiscent of the lines we would expect from the individual pulses in Eq. (18), as is illustrated in Fig. 6. Again, we see that the collection of waves depicted in this figure does not have a well-defined associated EDR.

### 3. *Effective dispersion relations of special multisolitonlike waves*

From the discussion at the end of the previous section, at first, it may seem unlikely that any multisolitonlike periodic wave could generate a parabolic EDR, since the lines

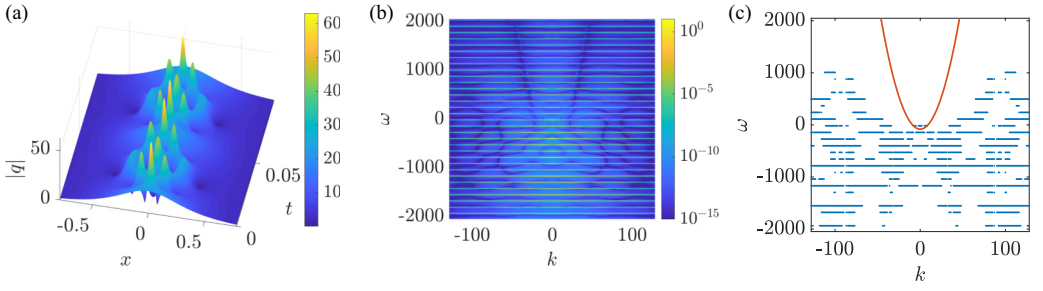


FIG. 5. Multi-"breather"-type wave generated from Eq. (19) with $M = 4$, $A = 4$, and $\alpha = 1$. The computational domain was $L = 2\pi$, with $N_x = 2^{12}$, $\Delta t = \Delta x^2/2\pi$, and a final time $T = \pi/2$. (a) Surface plot of the wave, displayed here at an angle to more clearly highlight the behavior of the breather, with color indicating the magnitude of the wave amplitude $|q(x,t)|$. (b) The spatiotemporal PSD of the wave, i.e., the argument on the right-hand side of Eq. (2), used in the WFS analysis, plotted using a logarithmic color scale. (c) Peak-frequency $\omega$ values for each wave number $k$ of the PSD in panel (b). Here, all the peaks of the PSD within 90% of the global peak value at every $k$ were marked with a blue dot. These peaks (blue) are compared with the relevant theoretically predicted parabolic EDR in Eq. (9) (red). Panels (b) and (c) were computed using the argument in Eq. (4) and employed averaging over 4 windows of width $T_{\text{win}} = \pi/8$.

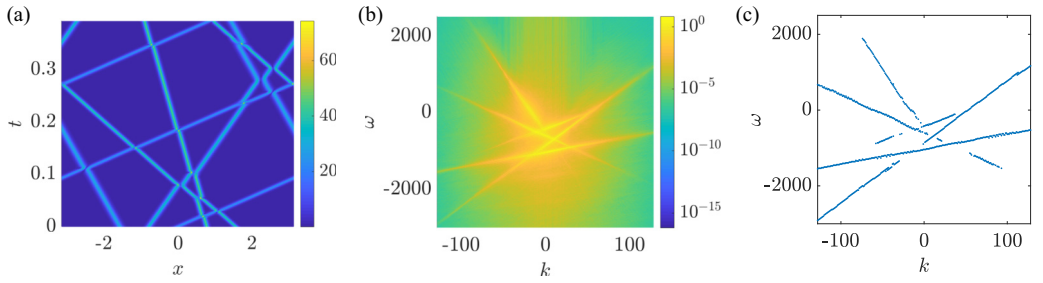


FIG. 6. FNLS wave consisting of five distinct pulses, with parameters $(A, V, \delta) = (20, -4, -\pi/2)$, $(24, 5, -\pi/4)$, $(16, 16, 0)$, $(32, -2, \pi/4)$, $(28, -8, \pi/2)$, and with $\alpha = 1$. The computational domain was $L = 2\pi$ with $N_x = 2^{11}$, $\Delta t = \Delta x^2/2\pi$, and a final time $T = \pi$. (a) Color contour plot of the solution with color indicating the magnitude of the wave amplitude $|q(x,t)|$. (b) The spatiotemporal PSD of the wave, i.e., the argument on the right-hand side of Eq. (2), used in the WFS analysis, plotted with a logarithmic color scale. (c) Peak-frequency $\omega$ values for each wave number $k$ of the PSD in panel (b). In contrast to previous examples, here we have used a blue dot to mark each peak of the PSD which is at least 10 times as high as its nearest local minimum value at every $k$. This is done so that all five pulses are diagnosed. In this example, the pulses, respectively, each contribute a line to the spectrum, where fitting these lines to $\omega = -(A^2 + V^2) - 2Vk$ result in $(A, V) = (20.06, -3.92)$, $(24.02, 5.004)$, $(16.42, 16.26)$, $(31.98, -2)$, $(27.99, -8.005)$, respectively. Panels (b) and (c) were computed using the argument Eq. (4) and employed averaging over 8 windows of width $T_{\text{win}} = \pi/8$.

corresponding to its individual constituent solitonlike pulses appear quite robust. Yet we can construct multisolitonlike, spatially periodic FNLS waves that do have parabolic EDRs. In particular, if we take a number of single-soliton-like pulses, initially spaced sufficiently far apart, and restrict them to all have the same peak amplitude $A$, while their velocities are

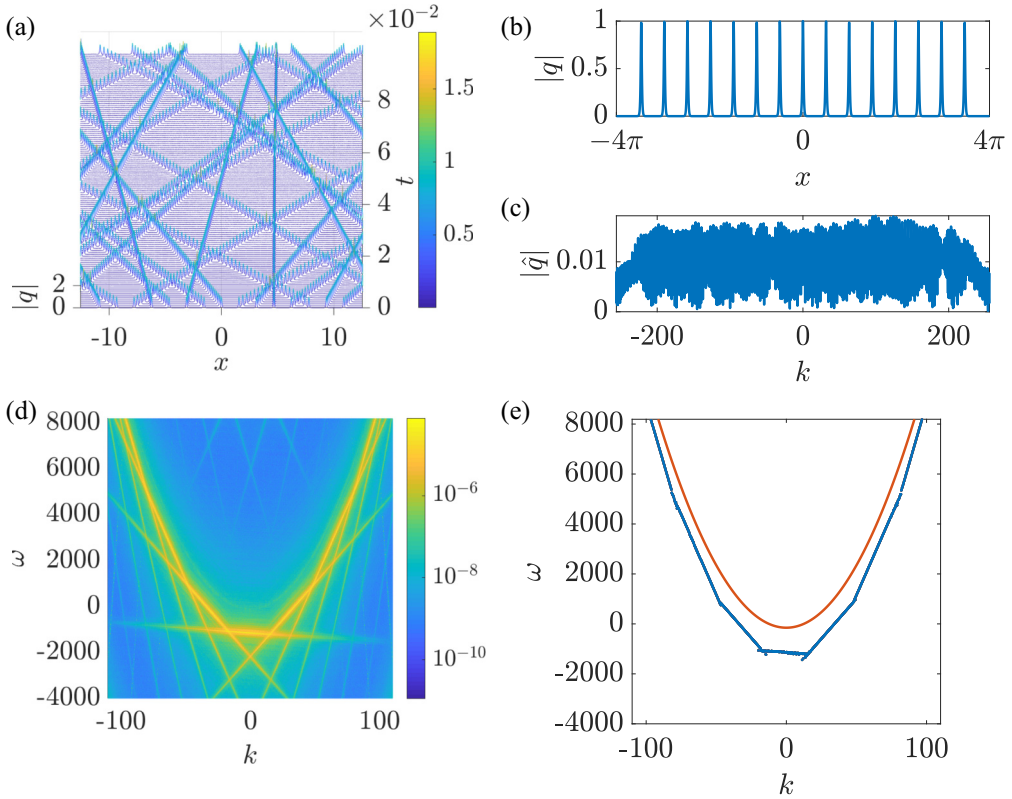


FIG. 7. FNLS wave consisting of 15 pulses, which are evenly distributed and well-separated across the spatial domain, as well as widely distributed in wave-number space. In particular, we sum 15 pulses of the form Eq. (14), with parameters $A = 32$, $\psi = 0$, $\alpha = \sqrt{2}A$, $\delta_j = \pm 13Lj/210$, $V_\ell = \pm 32\ell$. Pulse velocities were sorted randomly so $V_j$ need not correspond to $\delta_j$. The computational domain was $L = 8\pi$ with $N_x = 2^{12}$, $\Delta t = \Delta x^2/2\pi$, and a final time $T = \pi$. (a) Three-dimensional space-time profile of the wave at constant-time slices, where color indicates the wave amplitude $|q(x,t)|$. (b) The initial spatial wave profile at $t = 0$. (c) The wave-number dependence of the wave's Fourier amplitude $|\hat{q}(k,t)|$, defined in Eq. (3), at $t = 0$. (d) The spatiotemporal PSD of the wave, i.e., the argument on the right-hand side of Eq. (2), used in the WFS analysis, plotted with a logarithmic color scale. (e) EDR obtained according to the WFS analysis by finding the peak frequency $\omega$ values for each wave number $k$ of the PSD in panel (d). Here, all the peaks of the PSD within 1% of the global peak value at every $k$ were marked with a blue dot. The resulting EDR (blue) is compared with the theoretically predicted parabolic EDR in Eq. (9) (red). Panels (d) and (e) were computed using the argument in Eq. (4) and employed averaging over 4 windows of width $T_{\text{win}} = \pi/4$.

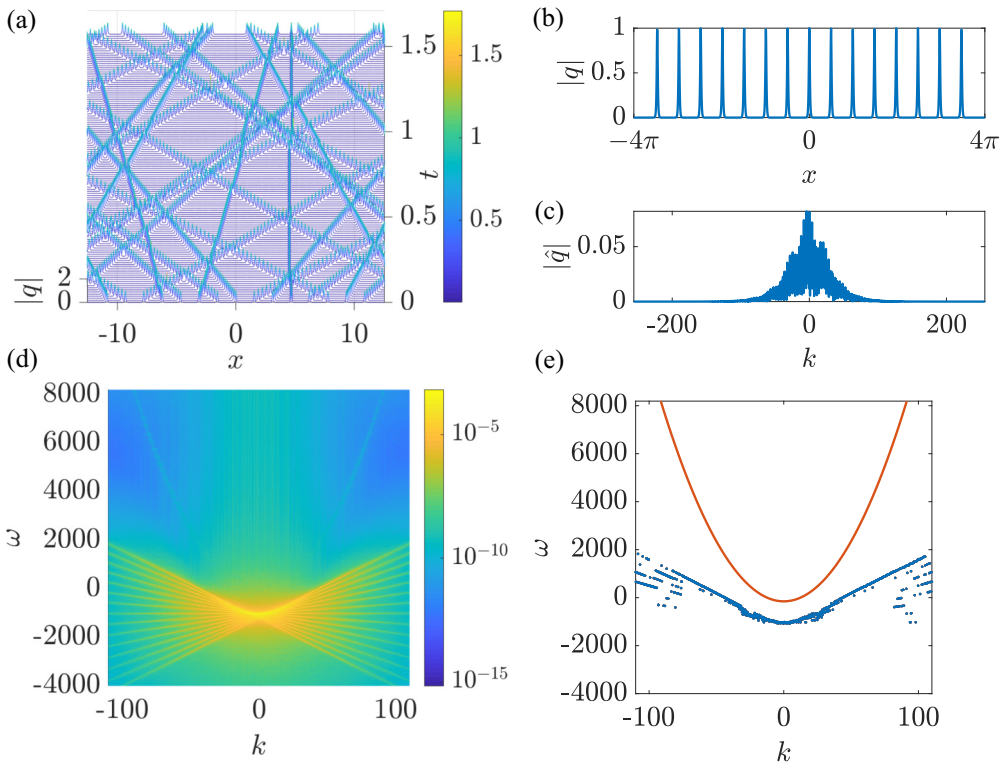


FIG. 8. FNLS wave consisting of 15 pulses, which are evenly distributed and well-separated across the spatial domain, but now narrowly distributed in wave-number space. In particular, we sum 15 pulses of the form Eq. (14), with parameters $A = 32$, $\psi = 0$, $\alpha = \sqrt{2}A$, $\delta_j = \pm 13Lj/210$, $V_\ell = \pm 2\ell$. Pulse velocities were sorted randomly so $V_j$ need not correspond to $\delta_j$. The computational domain was $L = 8\pi$ with $N_x = 2^{12}$, $\Delta t = \Delta x^2/2\pi$, and a final time $T = \pi$. (a) Three-dimensional space-time profile of the wave at constant-time slices, where color indicates the wave amplitude $|q(x,t)|$. Notice the difference in timescales between panel (a) of this figure and panel (a) of Fig. 7. (b) The initial spatial wave profile at $t = 0$. (c) The wave-number dependence of the wave's Fourier amplitude $|\hat{q}(k,t)|$, defined in Eq. (3), at $t = 0$. (d) The spatiotemporal PSD of the wave, i.e., the argument on the right-hand side of Eq. (2), used in the WFS analysis, plotted with a logarithmic color scale. (e) EDR obtained according to the WFS analysis by finding the peak frequency $\omega$ values for each wave number $k$ of the PSD in panel (d). Here, all the peaks of the PSD within 1% of the global peak value at every $k$ were marked with a blue dot. The resulting EDR (blue) is compared with the theoretically predicted parabolic EDR in Eq. (9) (red). Panels (d) and (e) were computed using the argument in Eq. (4) and employed averaging over 4 windows of width $T_{\text{win}} = \pi/4$.

picked randomly from the uniform distribution on a chosen interval, the EDR lines of these pulses are in fact tangent to a parabola, and their PSDs have their highest intensities at the points of tangency.

To explain the claim made in the previous paragraph, we notice that a straight-line EDR of a single FNLS soliton with amplitude $A$ and velocity $2V$, given by $\omega(k) = -(A^2 + V^2) - 2Vk$ in Eq. (18), is tangent to a parabola $\omega(k) = k^2 - C$ precisely when $C = A^2$, and tangency occurs at $k = -V$. Moreover, for this soliton, the PSD in Eq. (16) along the straight line EDR in Eq. (18) has sech-like intensity, centered at $k = -V$, i.e., at the tangency point between this line and the parabola $k^2 - A^2$.

Now, consider an initial group of $N$ solitonlike pulses, all with the same peak amplitude $A$, equally spaced far enough from one-another so that they do not overlap and can thus evolve as a multisolitonlike wave. Let their velocities $2V_j$, $j = 1, \ldots N$, also be equally spaced over the interval $-V_0 < V_j < V_0$, but assigned randomly to different pulse locations. Then, the EDR of the resulting wave comprises a collection of segments of the straight lines $\omega_j(k) = -(A^2 + V_j^2) - 2V_j k$, centered around $k = -V_j$, for $j = 1, \ldots, N$, which are all tangent to the parabola $k^2 - A^2$. In other words, this parabola is their envelope. For large $N$, the lengths of the segments shrink, and their parabolic envelope thus becomes indistinguishable from the EDR of the corresponding multisoliton solution, i.e., this EDR becomes

$$\omega(k) = k^2 - A^2. \tag{20}$$

Therefore, in this case, the EDR is indeed again a parabola, but now $k^2$ shifted downward by the square of the common peak amplitude of the wave's constituent solitonlike pulses.

Two different examples of such EDRs are illustrated in Figs. 7 and 8. In both cases, we use an initial condition of 15 spatially distinct pulses, all with the same peak amplitude parameter $A = 32$. Both spectra indicate straight lines corresponding to each pulse, with each line accurately corresponding to the appropriate EDR in Eq. (18). Clear parabolas are emerging as envelopes of these lines in each case. Note that neither of these is, however, the parabola of Eq. (9), since the corresponding waves are well approximated by multisolitonlike pulses. Instead, the EDRs of these waves are described by Eq. (20), as discussed in the previous paragraph.

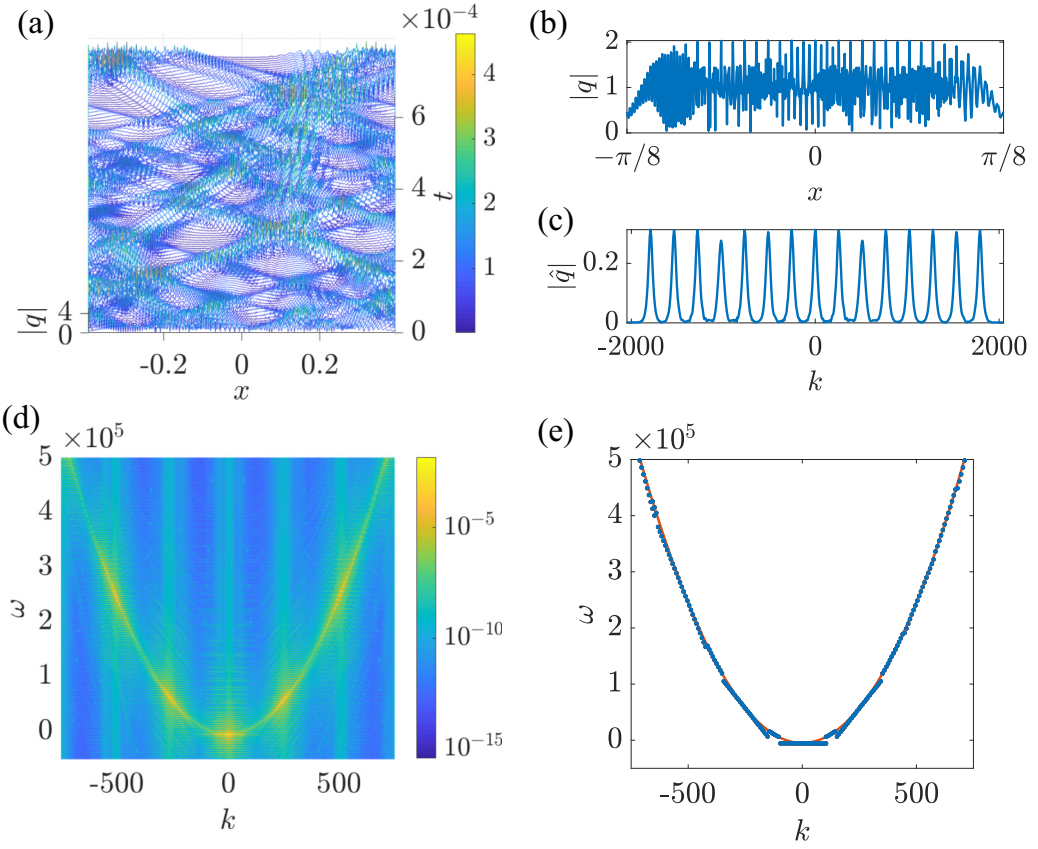


FIG. 9. FNLS wave consisting of 15 pulses, which are evenly distributed and narrowly separated across the spatial domain, but widely distributed in wave-number space. In particular, we sum 15 pulses of the form Eq. (14), with parameters $A = 32$, $\psi = 0$, $\alpha = \sqrt{2}A$, $\delta_j = \pm 13Lj/210$, $V_\ell = \pm 256\ell$. Pulse velocities were sorted randomly so $V_j$ need not correspond to $\delta_j$. The computational domain was $L = \pi/4$ with $N_x = 2^{10}$, $\Delta t = \Delta x^2/2\pi$ and a final time $T = \pi/16$. (a) Three-dimensional space-time profile of the wave at constant-time slices, where color indicates the wave amplitude $|q(x,t)|$. (b) The initial spatial wave profile at $t = 0$. (c) The wave-number dependence of the wave's Fourier amplitude $|\hat{q}(k,t)|$, defined in Eq. (3), at $t = 0$. (d) The spatiotemporal PSD of the wave, i.e., the argument on the right-hand side of Eq. (2), used in the WFS analysis, plotted with a logarithmic color scale. (e) EDR obtained according to the WFS analysis by finding the peak frequency $\omega$ values for each wave number $k$ of the PSD in panel (d). Here, all the peaks of the PSD within 1% of the global peak value at every $k$ were marked with a blue dot. Individual lines contained in the blue data were fit to equations of the type $\omega(k) = \omega_{j,0} - 2\tilde{V}_j k$ using least squares. A least-squares fit to the tangency points $(k_j = -\tilde{V}_j, \omega_j = \omega_{j,0} + 2\tilde{V}_j^2)$, as discussed in the text in Sec. III B 3, yields the parabolic EDR fit $\omega = k^2 - 5521$, which is compared with the theoretically predicted parabolic EDR in Eq. (9) $\omega = k^2 - 4857$ (shown in red). These two curves are indistinguishable on the scale of the plots in panels (d) and (e). See discussion in Sec. III B 3 for additional comments about panel (e). Panels (d) and (e) were computed using the argument in Eq. (4) and employed averaging over 4 windows of width $T_{\text{win}} = \pi/64$.

In Fig. 7, the constituent pulses' velocities $2V_j$ are distributed over a wide interval, so that the their corresponding straight-line EDRs in Eq. (18) are tangent to the parabolic EDR in Eq. (20) over a wide interval of wave numbers $k$. In Fig. 8, the pulses have a smaller range of values for the velocities $2V_j$, and so the tangencies of their straight-line EDRs to the parabola in Eq. (20) take place over a narrower range of wave numbers $k$. Note that the waves in Figs. 7 and 8 are very similar in appearance; however, note also that they evolve on quite different timescales due to their disparate velocity ranges.

We should remark that, in contrast to Figs. 7 and 8, where the initial pulses were sufficiently separated in space, when we choose the opposite extreme of overlapping initial pulses, a significant amount of radiationlike behavior is introduced because this initial profile is merely a sum of single-solitonlike pulses rather than a true exact multisolitonlike shape. Two different examples of this scenario are illustrated in Figs. 9 and 10. Again, in both cases we use an initial condition of 15 pulses, with the same peak amplitude parameter $A = 32$, but here the $x$-interval is a fraction of what it was in Figs. 7 and 8. Again, in Fig. 9, the pulses have a wide range of velocities $2V$ and in Fig. 10, the range for $V$ is small.

With the wide range of values for $V$ in Fig. 9, the spectrum indicates line segments that are distinct in wave number $k$, similar to the case shown in Fig. 7. However, these segments no longer correspond to the pulse parameters according to Eq. (18). Instead, as seen from panel (e) of Fig. 9, the segments are shifted vertically so as to be tangent to the parabola of Eq. (9), evidently because of the "radiation" introduced in the overlap between the initial pulses. In particular, they have the correct $V$, the slope that corresponds to the velocity of the pulse, but different $A$, the vertical intercept that corresponds to the amplitude of the pulse. With a smaller range of $V$

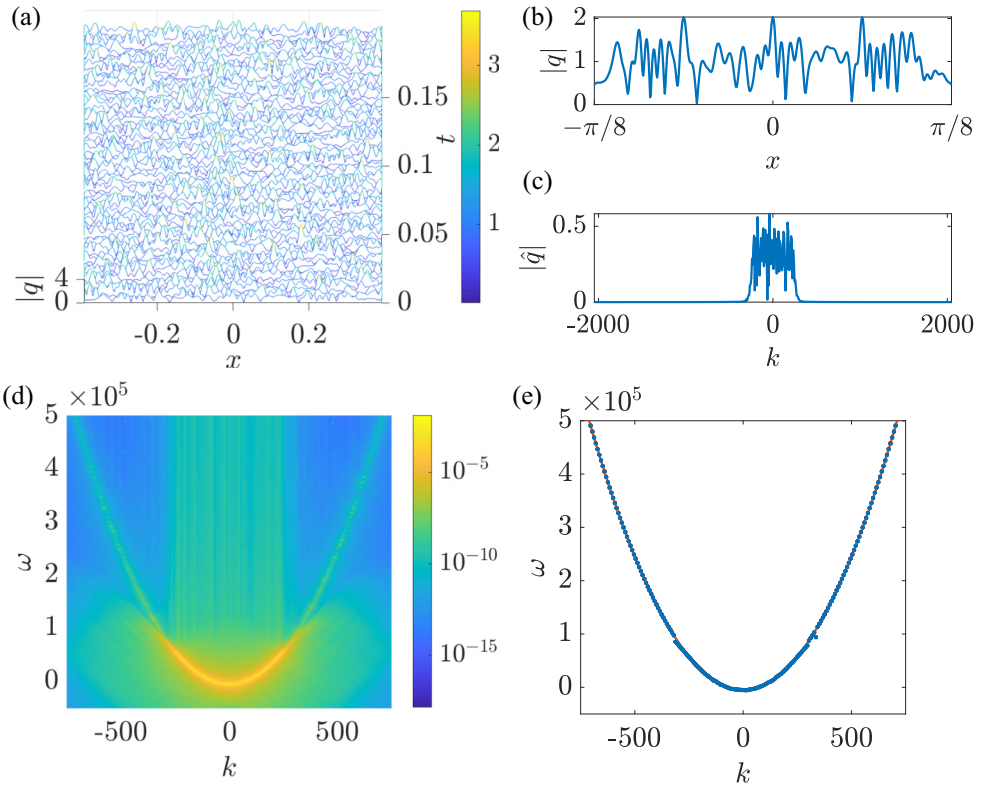


FIG. 10. FNLS wave consisting of 15 pulses, which are evenly distributed and narrowly separated across the spatial domain, and also narrowly distributed in wave-number space. In particular, we sum 15 pulses of the form Eq. (14), with parameters $A = 32$, $\psi = 0$, $\alpha = \sqrt{2}A$, $\delta_j = \pm 13Lj/210$, $V_\ell = \pm 32\ell$. Pulse velocities were sorted randomly so $V_j$ need not correspond to $\delta_j$. The computational domain was $L = \pi/4$ with $N_x = 2^{10}$, $\Delta t = \Delta x^2/2\pi$ and a final time $T = \pi/16$. (a) Three-dimensional space-time profile of the wave at constant-time slices, where color indicates the wave amplitude $|q(x,t)|$. (b) The initial spatial wave profile at $t = 0$. (c) The wave-number dependence of the wave's Fourier amplitude $|\hat{q}(k,t)|$, defined in Eq. (3), at $t = 0$. (d) The spatiotemporal PSD of the wave, i.e., the argument on the right-hand side of Eq. (2), used in the WFS analysis, plotted with a logarithmic color scale. (e) EDR obtained according to the WFS analysis by finding the peak frequency $\omega$ values for each wave number $k$ of the PSD in panel (d). Here, all the peaks of the PSD within 1% of the global peak value at every $k$ were marked with a blue dot. A least-squares fit to the blue data yields $\omega = k^2 - 5227$, which is compared with the theoretically predicted parabolic EDR in Eq. (9) $\omega = k^2 - 4762$ (red). These two curves are indistinguishable on the scale of the plots in panels (d) and (e). Panels (d) and (e) were computed using the argument in Eq. (4) and employed averaging over 4 windows of width $T_{\text{win}} = \pi/64$.

shown in Fig. 10, we do not even see the EDR lines of the initial pulses any more; all that remains is the parabola of Eq. (9), likely because the wave now appears to be dominated by "radiation." This scenario is also reflected in Figs. 9(a) and 10(a): the wave depicted in Fig. 9 still contains traces of the initial pulses, whereas the initial pulses in Fig. 10 have all but disappeared in a sea of what looks like dispersive ripples.

Waves that evolve from overlapping initial pulses, such as those discussed in the preceding two paragraphs, thus appear to belong to the robust family of waves studied in Sec. III A 2, or at least exhibit the same EDRs as waves that belong to this family. The two examples discussed in these two paragraphs also suggest that waves in that robust family can be thought of as dominated by "radiation," or at least as containing a substantial "radiation" component.

#### *4. Waves and coherent structures with ambiguous EDRs*

One last type of waves for which we seek an EDR comprises one or more coherent structures riding on top of a set of dispersive waves. For the first such wave, we choose the initial wave form composed of equidistant but overlapping soliton-shaped pulses shown in Fig. 9, and superimpose a soliton-shaped wave on top of it that is four times taller and narrower than the rest of the pulses. A tall coherent structure, traces of smaller pulses, and dispersive radiation waves are clearly visible in the resulting evolution. In the corresponding mode-dependent PSD of Fig. 11, a parabola satisfying Eq. (9) can be seen; however, its intensity is not uniform, and many straight lines are also present. The dominating straight line has the slope $V$ corresponding to the superimposed narrow soliton-shaped pulse, but its intercept $A$ is shifted. The parabola is also shifted slightly from the position described by Eq. (9). Both these curves appear to be moved due to the interaction of the pulse with the radiation components and possibly the smaller pulses contained in the wave. No single pronounced maximum of the PSD emerges for many wave numbers $k$, and so there appears to be no EDR. However, if we nonetheless take the location of the largest value of the PSD for each wave number $k$, then an EDR composed of straight-line and parabolic segments would emerge.

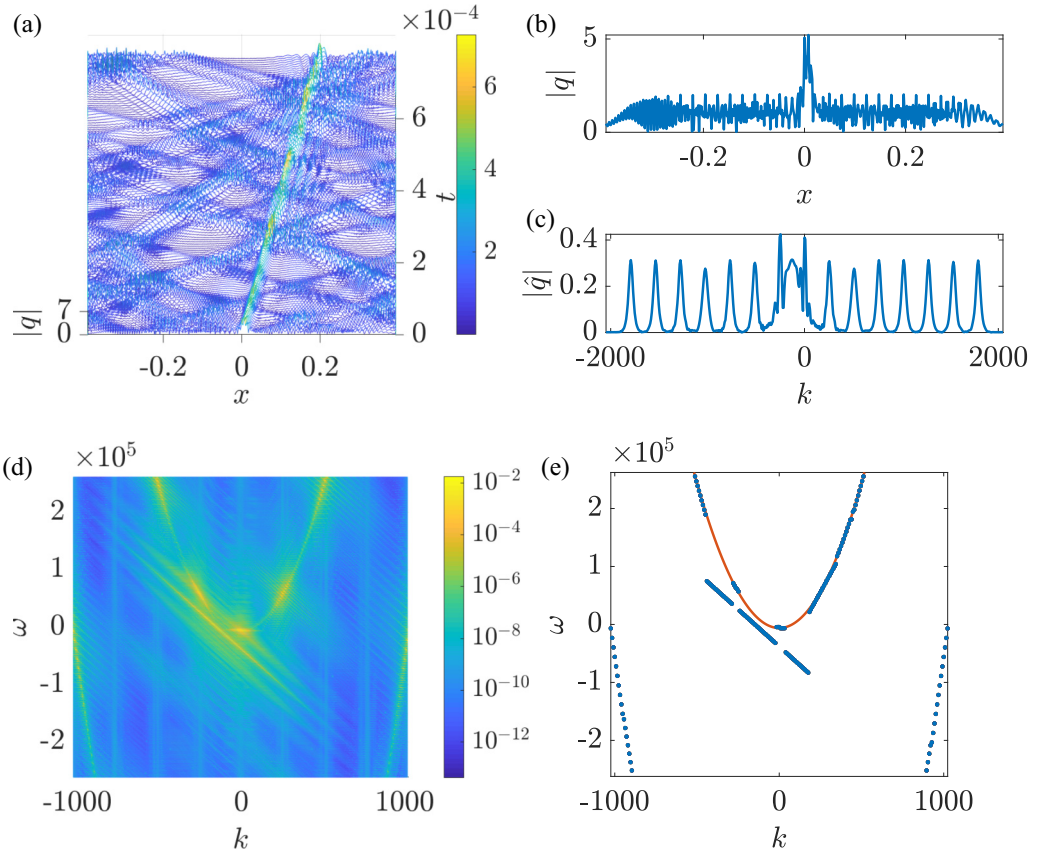


FIG. 11. FNLS wave generated from an initial condition of 15 equal size, identically spaced solitonlike pulses plus one tall, narrow solitonlike pulse. The parameters of the 15 pulses are the same as those used to compute Fig. 9. The additional pulse has the form given in Eq. (14), with parameters $A = 128$, $\psi = 0$, $\alpha = 32\sqrt{2}$, $\delta = \pm 13\pi/1680$, $V = 128$. The computational domain was $L = \pi/4$ with $N_x = 2^{10}$, $\Delta t = \Delta x^2/2\pi$ and a final time $T = \pi/16$. (a) Three-dimensional space-time profile of the wave at constant-time slices, where color indicates the wave amplitude $|q(x,t)|$. (b) The initial spatial wave profile at $t = 0$. (c) The wave-number dependence of the wave's Fourier amplitude $|\hat{q}(k,t)|$, defined in Eq. (3), at $t = 0$. (d) The spatiotemporal PSD of the wave, i.e., the argument on the right-hand side of Eq. (2), used in the WFS analysis, plotted with a logarithmic color scale. (e) EDR obtained according to the WFS analysis by finding the peak frequency $\omega$ values for each wave number $k$ of the PSD in panel (d). Here, all the peaks of the PSD within 1% of the global peak value at every $k$ were marked with a blue dot. The resulting EDR (blue) is compared with the theoretically predicted parabolic EDR in Eq. (9) (red). The EDR predicted by Eq. (9) is $\omega = k^2 - 6189$. The least-squares parabolic fit for small $k$, not including the line segments, gives the EDR of $\omega = k^2 - 8205$. The parabolic fit for large $k$ [of the periodically repeated parabola pieces on either side of panels (d) and (e)] gives EDR of $\omega = k^2 - 8740$. The fit for the dominant straight line, using all three line segments in the blue data, gives $A = 147$ and $V = 128$ in Eq. (18). Panels (d) and (e) were computed using the argument in Eq. (4) and employed averaging over 4 windows of width $T_{\text{win}} = \pi/64$.

Finally, we look at a wave evolved from an initial condition of a periodic, spatial random-walk-like wave form. (See Appendix E.) The amplitude values of the initial condition in different subregions of the interval $|x| < L/2$ dictate how many modes in that subregion become unstable, and the change of phase dictates the velocities of these unstable modes. This random initial wave evolves into a maze of meandering coherent structures, as seen in Fig. 12. The PSD computed for the WFS analysis, as displayed in Fig. 12(e), reveals the presence of a parabola satisfying Eq. (9), as well as line segments corresponding to a soliton. This wave again appears not to possess an unambiguous EDR. However, if, as in the previous example, we take the location of the largest value of the PSD for each wave number $k$, then the resulting EDR would again be discontinuous and follow the parabola for larger values of $k$, but other parts of it would appear linear.

## IV. CONCLUSIONS

In this article, we studied EDRs for different types of FNLS waves. The main result is that, for a robust family of waves, we found the parabolic EDR in Eq. (9), which equals the linear dispersion relation shifted downward by twice the total wave action of the wave multiplied by the square of the nonlinearity parameter. This EDR appears to have a universal form parallel to that predicted for long wave-modes and verified numerically for the general defocusing MMT model in Ref. [5], which includes the defocusing nonlinear Schrödinger equation.

That the general defocusing MMT form of the EDR is valid for waves of the nonlinear Schrödinger equation is a bit surprising, since this equation is an integrable system. That the same form of the EDR holds for a robust family of FNLS waves is still more surprising, since the FNLS additionally

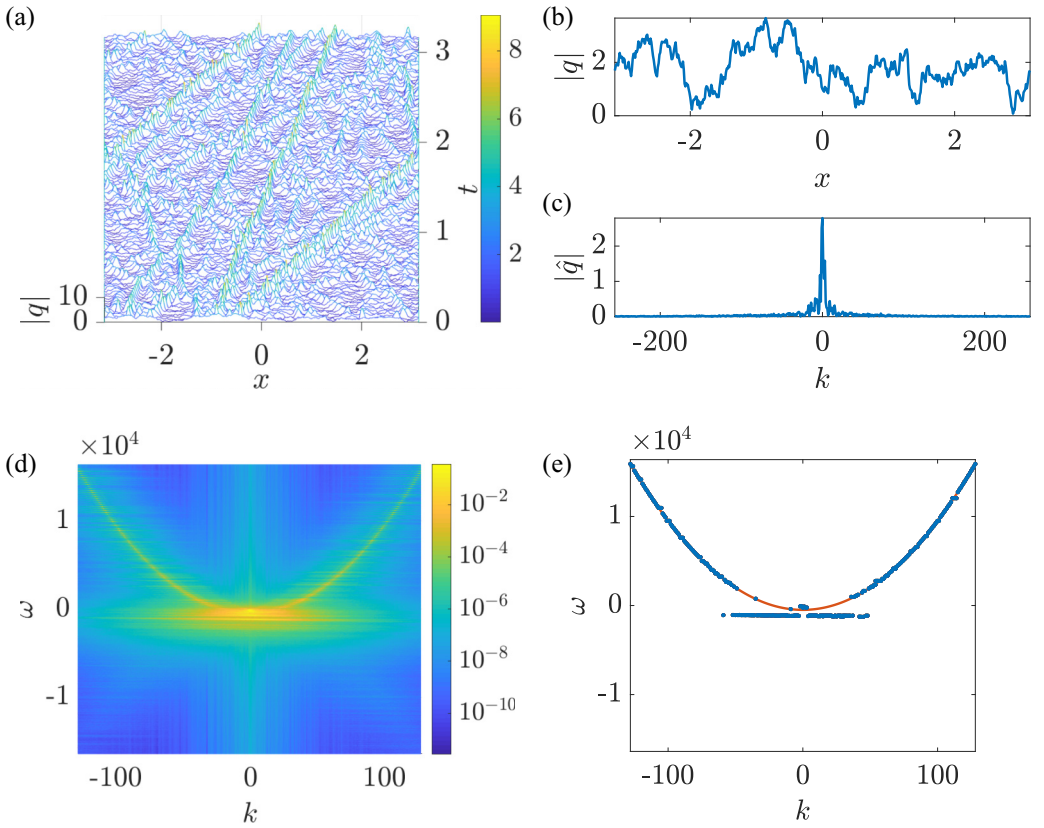


FIG. 12. FNLS wave generated from an initial condition of a (smoothed) periodic spatial random walk, as described in Appendix E. The nonlinearity parameter was $\alpha = 8$ and the computational domain was $L = 2\pi$ with $N_x = 2^{12}$, $\Delta t = \Delta x^2/2\pi$ and a final time $T = \pi$. (a) Three-dimensional space-time profile of the wave at constant-time slices, where color indicates the wave amplitude $|q(x,t)|$. (b) The initial spatial wave profile at $t = 0$. (c) The wave-number dependence of the wave's Fourier amplitude $|\hat{q}(k,t)|$, defined in Eq. (3), at $t = 0$. (d) The spatiotemporal PSD of the wave, i.e., the argument on the right-hand side of Eq. (2), used in the WFS analysis, plotted with a logarithmic color scale. (e) EDR obtained according to the WFS analysis by finding the peak frequency $\omega$ values for each wave number $k$ of the PSD in panel (d). Here, all the peaks of the PSD within 1% of the global peak value at every $k$ were marked with a blue dot. The resulting EDR (blue) is compared with the theoretically predicted parabolic EDR in Eq. (9) (red). The EDR predicted by Eq. (9) is $\omega = k^2 - 489$; the fit of the parabolic part of the blue data for $|k| > 60$ gives EDR of $k^2 - 487$. Panels (d) and (e) were computed using the argument in Eq. (4) and employed averaging over 4 windows of width $T_{\text{win}} = \pi/4$.

exhibits instabilities and generates coherent structures such as (multi)solitons. Yet, clearly, our derivation of this EDR in the case of small nonlinearity and its derivation in Ref. [24] in the case of small amplitudes of the modes, as well as its numerical confirmation in example FNLS waves obtained using a variety of techniques from a variety of initial-condition families, give strong evidence in favor of extending the validity of the predictions in Ref. [5] also to the focusing regime and the exceptional integrable structure of the FNLS.

Nevertheless, the integrable structure of the FNLS and the presence of coherent structures do exhibit their effects, as the FNLS gives rise to both waves with no EDR at all, waves with EDRs other than a quadratic function of the wave number, as well as a family of waves with a quadratic EDR which equals neither that in Eq. (9) nor the linear dispersion relation. In particular, why the form of this latter EDR should still be a quadratic, although we have been able to derive it explicitly for a specific type of multisolitonlike wave trains, remains a bit of a mystery.

Examples of observed or experimentally measured EDRs range over fields as diverse as surface gravity [41] and gravity-capillary waves [42], nonlinear springs [43], ionization waves [44], and graphene sheets [45]. Reference [42] presents a particularly striking example of an EDR with several distinct branches whose number depends on the amount of power injected into the waves. While none of these measurements have addressed EDRs for the FNLS discussed here, experimental data yielding these EDRs may perhaps be obtained from observations and measurements of random and rogue waves in wave tanks [46,47] and optics [48]. These are approximately described by the FNLS, and our results may apply to them.

One remaining open theoretical problem is to extend the mathematically rigorous result of Ref. [24] from the limit of small amplitudes of the modes to at least some of the more general cases described here using numerical simulations. Another concerns the precise role of integrability in the existence and form of the EDR in Eq. (9). Perhaps the Fourier representation of the theta-function FNLS solutions may help in this regard [49].

Finally, as mentioned in the Introduction, the existence of an EDR for a wave of the FNLS signifies that this wave is,

statistically, a collection of weakly nonlinearly coupled plane waves whose long-term time-evolution is dominated by this EDR. Therefore, for such a wave, splitting either the FNLS equation or its total energy into effective linear and nonlinear parts based on this EDR should result in minimizing the latter part. In addition, the question arises as to what the relative sizes of the two effective parts are, and which part dominates for large values of the nonlinearity parameter. We will address these issues in a subsequent publication.

## ACKNOWLEDGMENTS

We are grateful to G. Biondini, K. Newhall, M. Schwartz, and V. Zharnitsky for helpful discussions. K.L. was partly supported by the U.S. Department of Education Graduate Assistance in Areas of National Need (GAANN), the NSF Research Training Group Grant No. DMS-0636358, and the NSF Research Training Group Grant No. DMS-1344962. G.K. was partly supported by the NSF Grant No. DMS-1615859. J.W.B. was partly supported by a U.S. Presidential Early Career Award for Scientists and Engineers. J.W.B. and G.K. were partly supported by a Simons foundation grant for collaboration on weak turbulence. D.Z. was partly supported by National Science Foundation of China with Grants No. 11671259, No. 11722107, and No. 91630208. D.C. was partly supported by National Science Foundation of China with Grant No. 31571071. D.Z. and D.C. were partly supported by NYU Abu Dhabi Institute Grant No. G1301 and the SJTU-UM Collaborative Research Program.

## APPENDIX A: SOLUTION OF THE FNLS VIA INVERSE-SCATTERING TRANSFORM

In this Appendix, we give a brief, heuristic review of the inverse scattering transform applied to the FNLS to obtain waves comprising solitons and radiation. In our exposition, we largely follow the exposition in Ref. [22]. Classic references are Refs. [17,18,20]. We took the notation from Ref. [50]. We purposely ignore any questions of analyticity.

The FNLS in Eq. (1), with the dependent variable $q$ rescaled so that $\alpha = \sqrt{2}$, is the compatibility condition for the Lax Pair

$$\phi_x = (ik\sigma_3 + Q)\phi, \tag{A1a}$$

$$\phi_t = (2ik^2\sigma_3 + H)\phi, \tag{A1b}$$

where

$$\sigma_3 = \begin{bmatrix} 1 & 0 \\ 0 & -1 \end{bmatrix}, \quad Q = \begin{bmatrix} 0 & q \\ r & 0 \end{bmatrix}, \tag{A1c}$$

$$H = iQ^2\sigma_3 + iQ_x\sigma_3 + 2kQ, \tag{A1d}$$

and $r = -q^*$. Equation (A1a) is called the scattering equation and Eq. (A1b) is the evolution equation.

The scattering equation in Eq. (A1a) has eigenfunction solutions that satisfy asymptotic boundary conditions:

$$\phi^{\pm}(x,t,k) \sim e^{ik\sigma_3 x}, \quad x \to \pm\infty. \tag{A2}$$

Because the eigenfunctions $\phi^{\pm}$ are both fundamental matrix solutions of Eq. (A1a), we can write a "scattering" relation between them in the form

$$\phi^{+}(x,t,k) = \phi^{-}(x,t,k)\,S(t,k), \tag{A3}$$

where $S$ is the $2 \times 2$ scattering matrix with elements $s_{ij}$. One can show that the coefficients of the scattering matrix satisfy the symmetry

$$s_{22}(t,k) = s_{11}^*(t,k^*), \quad s_{12}(t,k) = -s_{21}^*(t,k^*), \tag{A4}$$

which implies that $S$ is unitary for real values of the spectral parameter $k$. One can also show that the element $s_{11}(t,k)$ of the scattering matrix is time-independent. The coefficients in the asymptotic expansion of $\ln s_{11}(t,k)$ in terms of $1/k$ give an infinite number of conserved quantities.

In terms of the individual columns, $\phi_1^{\pm}$ and $\phi_2^{\pm}$ of the matrix eigenfunctions $\phi^{\pm}$, Eq. (A3) can be rewritten as

$$\phi_1^{+} = s_{11}\phi_1^{-} + s_{21}\phi_2^{-}, \quad \phi_2^{+} = s_{12}\phi_1^{-} + s_{22}\phi_2^{-}. \tag{A5}$$

If, for real $k$, we rewrite the first equation in Eq. (A5) in the form

$$\frac{\phi_1^{+}}{s_{11}} = \phi_1^{-} + b(k,t)\,\phi_2^{-},$$

where $b(t,k) = s_{21}/s_{11}$, then we arrive at the interpretation in which $\phi_1^{-}$ represents a right-moving incoming wave and $b(t,k)\,\phi_2^{-}$ the corresponding reflected wave as $x \to -\infty$, and $\phi_1^{+}/s_{11}$ represents the transmitted wave as $x \to \infty$. Because of this interpretation, $b(k,t)$ is referred to as the reflection coefficient. [The same interpretation is obtained from the second equation in Eq. (A5) due to the symmetries in Eq. (A4).]

Likewise, for complex values $\zeta_j = \mathrm{Re}\zeta_j + i\,\mathrm{Im}\zeta_j$ of $k$ in the upper half-plane such that $s_{11}(0,\zeta_j) = 0$, and therefore $s_{11}(t,\zeta_j) = 0$ for all times $t$, we find a proportionality, $\phi_1^{+}(x,t,\zeta_j) = c_j(t)\phi_2^{-}(x,t,\zeta)$. In other words, we obtain an eigenfunction that decays exponentially at the rate $e^{-\mathrm{Im}\zeta|x|}$ at both $x \to \pm\infty$ and corresponds to the discrete eigenvalue $\zeta_j$ of the scattering equation in Eq. (A1a). In particular, if the decay rate as $x \to \infty$ is exactly $e^{-\mathrm{Im}\zeta_j x}$, it is $c_j(t)e^{\mathrm{Im}\zeta_j x}$ as $x \to -\infty$, and so $c_j(t)$ is referred to as the corresponding norming constant.

Using the asymptotics of the evolution equation in Eq. (A1b), we obtain the time evolution of the reflection coefficients and norming constants as

$$b(t,k) = e^{-4ik^2t}b_0(k), \quad c_j(t) = e^{-4i\zeta_j^2 t}c_j(0). \tag{A6}$$

Typically, we assume that there is a finite number $J$ of zeros $k = \zeta_j$ of $s_{11}(0,k)$ and that none of them lie on the real axis.

We reconstruct the FNLS wave $q(x,t)$ using the functions $\mu^{\pm}(x,t,k) = \phi^{\pm}(x,t,k)e^{-ik\sigma_3 x}$. In particular, $q$ is expressed as

$$q(x,t) = \lim_{k\to\infty} 2ik\mu_{12}^{-}(x,t,k). \tag{A7}$$

Using the techniques from the theory of Riemann-Hilbert problems, we can find equations for the entries $\mu_{11}^{-}$ and $\mu_{12}^{-}$. If we assume that the zeros of $s_{11}(0,k)$ at all the eigenvalues $k = \zeta_j$ are simple, and write $C_j = c_j(0)/s_{11}'(\zeta_j)$, then these

equations are

$$\mu_{11}^{-}(x,t,k) = 1 + \sum_{j=1}^{J} \frac{C_j e^{-2i\zeta_j x - 4i\zeta_j^2 t}\mu_{12}^{-}(x,t,\zeta_j)}{k-\zeta_j} + \frac{1}{2\pi i}\int_{-\infty}^{\infty} \frac{b_0(\lambda)e^{-2i\lambda x - 4i\lambda^2 t}\mu_{12}^{-}(x,t,\lambda)}{\lambda-(k-i\,0)}d\lambda, \tag{A8a}$$

$$\mu_{12}^{-}(x,t,k) = -\sum_{j=1}^{J} \frac{C_j^* e^{2i\zeta_j^* x + 4i\zeta_j^{*2} t}\mu_{11}^{-}(x,t,\zeta_j^*)}{k-\zeta_j^*} + \frac{1}{2\pi i}\int_{-\infty}^{\infty} \frac{b_0^*(\lambda)e^{2i\lambda x + 4i\lambda^2 t}\mu_{11}^{-}(x,t,\lambda)}{\lambda-(k+i\,0)}d\lambda. \tag{A8b}$$

Here, $\pm i\,0$ indicates the indentation direction of the integration path around the singularity at $\lambda = k$.

Using Eq. (A7), we obtain from Eqs. (A8) the wave $q$. After rescaling back to the original variables of the FNLS equation in Eq. (1), we find

$$q(x,t) = -\frac{2i\sqrt{2}}{\alpha}\left[\sum_{j=1}^{J} C_j^* e^{2i\zeta_j^* x + 4i\zeta_j^{*2} t}\mu_{11}^{-}(x,t,\zeta_j^*) - \frac{1}{\pi}\int_{-\infty}^{\infty} b_0^*(\lambda)e^{2i\lambda x + 4i\lambda^2 t}\mu_{11}^{-}(x,t,\lambda)d\lambda\right]. \tag{A9}$$

We obtain (multi)soliton solutions when the reflection coefficient vanishes, i.e., when $b_0(k) \equiv 0$. In particular, for the single soliton, when $J = 1$ and $\zeta_1 = (V + iA)/2$, Eqs. (A8) and (A9) yield the wave in Eq. (14). In general, the discrete sum in Eq. (A9) corresponds to the solitons, and the integral to the continuous radiation.

## APPENDIX B: EFFECTIVE DISPERSION RELATION FOR WEAK NONLINEARITY

In this Appendix, we apply the method of multiple scales to derive the EDR when the FNLS nonlinearity parameter $\alpha$ is small. We first transform the FNLS to the wave-number space by letting

$$q(x,t) = \sum_{n=-\infty}^{\infty} a_{k_n}(t)e^{-ik_n x}, \tag{B1}$$

with $k_n = 2\pi n/L$, in Eq. (1). We thus obtain the infinite set of ordinary differential equations

$$i\dot{a}_{k_n}(t) = -k_n^2 a_{k_n}(t) + \alpha^2 \sum_{p,q,r=-\infty}^{\infty} a_{k_p}(t)a_{k_q}(t)a_{k_r}^*(t)\delta_{k_p+k_q-k_r-k_n,0} \tag{B2}$$

for the wave modes $a_{k_n}(t)$, where $\delta_{j,l}$ is the Kronecker $\delta$.

The solution of Eq. (B2) assumes the wave-mode time form $a_{k_n}(t) = b_{k_n}(\alpha^2 t)e^{ik_n^2 t} + \alpha^2 a_{k_n,1}$, where $b_{k_n}(\alpha^2 t)$ satisfy the solvability condition

$$i\partial_{\alpha^2 t} b_{k_n} = \sum_{p,q,r=-\infty}^{\infty} b_{k_p} b_{k_q} b_{k_r}^* e^{i(k_p^2+k_q^2-k_r^2-k_n^2)t} \times \delta_{k_p+k_q-k_r-k_n,0}\,\delta_{k_p^2+k_q^2-k_r^2-k_n^2,0}. \tag{B3}$$

It is well known that the equations

$$k_p + k_q - k_r - k_n = 0,$$
$$k_p^2 + k_q^2 - k_r^2 - k_n^2 = 0$$

can only be solved if $p = r$ and $q = n$ or $p = n$ and $q = r$ [9]. Therefore, Eq. (B3) becomes

$$\partial_{\alpha^2 t} b_{k_n} = \left(2\sum_{m=-\infty}^{\infty} |b_{k_m}|^2 - |b_{k_n}|^2\right) b_{k_n}. \tag{B4}$$

Because

$$\sum_{m=-\infty}^{\infty} |b_{k_m}|^2 = \sum_{m=-\infty}^{\infty} |a_{k_m}|^2 = \|a_\kappa\|^2$$

is the conserved total wave action, the solution to Eq. (B4) equals

$$b_{k_n} = a_{k_n}(0)e^{i(2\|a_\kappa\|^2 - |a_{k_n}(0)|^2)\alpha^2 t},$$

which gives Eq. (6). The second equality in Eq. (9) is a consequence of Parseval's equality [51].

Here, we also comment on the remark made in Sec. III A 1 after Eq. (8) about the mode amplitudes $|a_{k_n}(0)|$ being conserved on $O(\alpha^{-2})$ timescales for small $\alpha$. This is connected to the complete integrability of the FNLS equation [17,18,20,22] (see Appendix A), whose consequence is that waves composed of modes with sufficiently small amplitudes, so as to avoid the modulational instability [cf. Eq. (13)], should be representable in terms of action-angle coordinates (cf. Refs. [17–19,35,39]). In particular, the actions should reduce to the mode amplitudes $|a_{k_n}(0)|$ in the limit of small nonlinearity, and the frequencies of the angles to the frequencies in Eq. (8). In this respect, intuitively, both the results of Sec. III A 1 as well as those of Ref. [24] should be expected. To our knowledge, however, a rigorous proof of the results of Ref. [24] via action-angle variables is yet to be developed.

## APPENDIX C: THE LIMIT OF SMALL AMPLITUDES OF THE MODES

In this Appendix, we describe the connection between our results and those obtained in Ref. [24] in the small-wave-amplitude limit.

In Ref. [24], the FNLS is scaled so that the factor 2 appears in Eq. (1) in place of the nonlinearity size $\alpha^2$. In this case, our limit of weak nonlinearity, discussed in Sec. III A 1 and Appendix B, can be replaced by the limit of small amplitude, which we again denote by $\alpha$. In this limit, the expansion in Eq. (6) must be replaced by one that acquires an overall factor proportional to $\alpha$, but otherwise remains the same. The necessary validity condition for this new expansion, i.e., the condition that none of its modes become modulationally unstable, is a reinterpretation of the weak-nonlinearity condition

in Eq. (13) in the form that all the mode amplitudes should be much smaller than $\pi/L$.

If we define the wave-modes $a_{k_n}(t)$ as in Eq. (B1), then the condition for the small-wave-amplitude limit considered in Ref. [24] states that all the initial wave-modes be small,

$$a_{k_n}(0) = O(\alpha), \tag{C1}$$

where $\alpha$ is again a small parameter. In this limit, the $L_2$ norm of the difference between the evolving FNLS wave $q(x,t)$ and the linear wave evolving according to the effective dispersion relation $k^2 - (4/L)\|q(x,0)\|_2^2$ in Eq. (9) (with the scaling of Ref. [24]) was shown to remain within $O(\alpha^2)$ for short times $t$ and $O(t\alpha^2)$ for long times. This result appears much stronger than what we claim to see numerically in the more general case, and states that the FNLS wave and its linear approximation using the EDR in Eq. (9) remain close on timescales shorter than $O(\alpha^{-2})$. However, these waves are probably not uniformly close nor have they close spatial slopes. Our claim, in turn, is only that the dynamics of each mode in a more general FNLS wave is dominated by a single frequency obeying the EDR in Eq. (9).

We should comment that the condition in Eq. (C1) certainly includes the small-amplitude limit, and thus, after a rescaling, also the weak-nonlinearity limit, but that it is more general. In particular, by containing an increasing number, $O(1/\alpha^2)$, of nondecaying modes of size $O(\alpha)$, a wave satisfying this condition may retain a total wave action, and thus $L_2$ norm, of size $O(1)$.

The result of Ref. [24] was proven in a mathematically rigorous manner using the Poincaré-Birkhoff normal form [52], a perturbation method formally equivalent to the method of multiple scales but more suitable for rigorous proofs [53,54]. Our numerical results show that the weaker, statistical interpretation of the EDR in Eq. (9) extends far beyond its proven validity in Ref. [24]. In particular, this EDR is valid for numerous waves with mode sizes of $O(1)$, including those resulting from modulational instability. We suspect that this instability may present a hard obstacle for the near-identity transformations leading to the normal form, and that any future rigorous proofs of the EDR form in Eq. (9) holding for waves with mode sizes of $O(1)$ may have to use different techniques.

## APPENDIX D: LINEAR-STABILITY ANALYSIS OF PLANE WAVES

In this Appendix, we apply linear stability analysis to the single plane wave solution of the FNLS, seeking to understand the behavior of its small perturbations [25–27]. We consider a perturbed wave $q(x,t) = \mathring{q}(x,t)[1+\epsilon(x,t)]$, where $\mathring{q}(x,t) = Ae^{-i[\gamma x - (\gamma^2 - |A|^2\alpha^2)t]}$ is a plane wave in Eq. (10) and $|\epsilon|^2 \ll 1$ is a small perturbation. We insert this ansatz into the FNLS and neglect higher-order terms in $\epsilon$ to obtain a partial differential equation for $\epsilon$:

$$i(\epsilon_t + 2\gamma\epsilon_x) = \epsilon_{xx} + |A|^2\alpha^2(\epsilon + \epsilon^*). \tag{D1}$$

We substitute plane-wave solutions

$$\epsilon(x,t) = \rho e^{i(kx-\omega t)} + \sigma e^{-i(kx-\omega^* t)} \tag{D2}$$

into Eq. (D1), noting that the frequency $\omega$ could be real (giving bounded, oscillating solutions) or complex (giving exponentially growing or decaying solutions).

Substituting the plane waves in Eq. (D2) into Eq. (D1), separately collecting terms with $e^{i(kx-\omega t)}$ and $e^{-i(kx-\omega^* t)}$, and taking the complex conjugate of the coefficients multiplying $e^{-i(kx-\omega^* t)}$ leads to the homogeneous linear algebraic system of equations for the coefficients $\rho$ and $\sigma^*$,

$$(\omega - 2\gamma k + k^2 - |A|^2\alpha^2)\rho - |A|^2\alpha^2\sigma^* = 0, \tag{D3a}$$

$$|A|^2\alpha^2\rho + (\omega - 2\gamma k - k^2 + |A|^2\alpha^2)\sigma^* = 0. \tag{D3b}$$

For this system to have nonzero solutions $\rho$ and $\sigma^*$, its determinant of coefficients must vanish, resulting in the following quadratic equation for $\omega$:

$$\omega^2 - 4\gamma k\omega + 4\gamma^2 k^2 - k^2(k^2 - 2|A|^2\alpha^2) = 0. \tag{D4}$$

When $k_n = 2\pi n/L$, we compute the following expressions for the two corresponding frequencies:

$$\omega_{\pm n} = 2\gamma k_n \pm k_n\sqrt{k_n^2 - 2|A|^2\alpha^2}. \tag{D5}$$

The frequencies in Eq. (D5) contain nonzero imaginary parts corresponding to an unstable mode precisely when $|k_n| < \sqrt{2}|A|\alpha$. An initial plane wave with amplitude $A$ propagating in spatial domain $|x| < L/2$ with nonlinearity parameter $\alpha$ will thus give rise to $2N+1$ unstable Fourier modes, where $N$ is as stated in Eq. (11). Note that the case $N = 0$ is excluded by the conservation of the total wave action.

## APPENDIX E: RANDOM SPATIAL INITIAL CONDITIONS

We generate spatially random, noiselike initial conditions in such a way that they appear disordered on $O(1)$ spatial scales, but are smooth on $O(\Delta x)$ spatial scales, where $\Delta x$ is the size of the spatial discretization interval used in our FNLS simulations. This is so that these initial conditions can be used in our simulations and not destroy the order of accuracy of the algorithms.

To generate an initial wave-form of (smoothed) spatial "white noise," at each spatial discretization point $x_j$, we define two normally distributed random variables $\rho_j$ and $\phi_j$, $j = 1,\ldots,N_x$, where $N_x$ is the number of spatial discretization points. We take for the initial wave-form the expression $q(x_j,0) = a(x_j) + ib(x_j)$, where

$$a(x_j) = 16\sum_{n=j-4}^{j+4}\rho_n, \quad b(x_j) = 16\sum_{n=j-4}^{j+4}\phi_n.$$

Here, we assume the periodicity $\ell \pm N_x \equiv \ell$.

To simulate a spatially periodic, (smoothed) "random-walk"-like initial wave-form, we again begin with two normally distributed random sequences $\rho_j$ and $\phi_j$, $j = -J,\ldots,J$, $j \neq 0$, and define the initial condition as [55]

$$q(x,0) = q_0\left[\sum_{\substack{j=-J\\ j\neq 0}}^{J}\frac{\rho_j + i\phi_j}{j}\,e^{2\pi ijx/L} + \rho_0 + i\phi_0\right],$$

where $q_0$ is the overall amplitude, and $\rho_0 + i\phi_0$ is chosen to determine the average value of $q(x,0)$. To preserve smooth-

ness on the spatial discretization scale, $O(\Delta x)$, we must take $N_x \gg 2J$. For our example in Sec. III B 4 and Fig. 12, we took $q_0 = 1/\sqrt{2}$, $\rho_0 + i\phi_0 = -0.6909 - 1.4166\,i$, $L = 2\pi$, $J = 2^8$, and $N_x = 2^{12}$.

## APPENDIX F: POWER-SPECTRAL DENSITY OF ONE SOLITON

To derive the wave-number dependence of the PSD for the single soliton $q(x,t)$ in Eq. (14), we first calculate its spatial Fourier transform $\hat{q}(k,t)$ via Eq. (3). Using the well-known formula

$$\int_{-\infty}^{\infty} \operatorname{sech}\xi\, e^{-i\kappa\xi}\, d\xi = \pi \operatorname{sech}\left(\frac{\pi\kappa}{2}\right),$$

we evaluate $\hat{q}(k,t)$ to be

$$\hat{q}(k,t) = \mathscr{A}(k) e^{-i\Omega(k)t}, \tag{F1}$$

where

$$\mathscr{A}(k) = \frac{\sqrt{2}\pi}{\alpha} \operatorname{sech}\frac{\pi(V+k)}{A} e^{i[\psi-(V+k)\delta]}, \tag{F2}$$

and $\Omega(k)$ is given in Eq. (17).

The finite-interval temporal Fourier transform of the mode in Eq. (F1) equals

$$\int_0^T \hat{q}(k,t) e^{-i\omega t}\, dt = i\mathscr{A}(k) e^{-i[\Omega(k)+\omega]T/2} \frac{\sin[(\Omega(k)+\omega)T/2]}{(\Omega(k)+\omega)/2},$$

which, together with Eqs. (F2) and (17) makes the expression for the PSD inside the argument on the right-hand side of Eq. (2) equal to that in Eq. (16).


[1] V. Zakharov, V. L'vov, and G. Falkovich, *Kolmogorov Spectra of Turbulence I—Wave Turbulence* (Springer, Berlin, 1992).
[2] G. B. Whitham, *Linear and Nonlinear Waves* (John Wiley & Sons, New York, 1974).
[3] B. Gershgorin, Y. V. Lvov, and D. Cai, Phys. Rev. Lett. **95**, 264302 (2005).
[4] B. Gershgorin, Y. V. Lvov, and D. Cai, Phys. Rev. E **75**, 046603 (2007).
[5] W. Lee, G. Kovačič, and D. Cai, Phys. Rev. Lett. **103**, 024502 (2009).
[6] W. Lee, G. Kovačič, and D. Cai, Proc. Natl. Acad. Sci. USA **110**, 3237 (2013).
[7] S.-x. W. Jiang, H.-h. Lu, D. Zhou, and D. Cai, Phys. Rev. E **90**, 032925 (2014).
[8] S. Jiang, H. Lu, D. Zhou, and D. Cai, New J. Phys. **18**, 083028 (2016).
[9] A. Majda, D. McLaughlin, and E. Tabak, J. Nonlin. Sci. **7**, 9 (1997).
[10] D. Cai, A. Majda, D. McLaughlin, and E. Tabak, Proc. Natl. Acad. Sci. USA **96**, 14216 (1999).
[11] D. Cai, A. J. Majda, D. W. McLaughlin, and E. G. Tabak, Physica D **152**, 551 (2001).
[12] Y. Wakata, J. Oceanogr. **63**, 483 (2007).
[13] J. T. Farrar, J. Phys. Oceanogr. **38**, 1669 (2008).
[14] T. Shinoda, G. N. Kiladis, and P. E. Roundy, Atmos. Res. **94**, 37 (2009).
[15] T. Shinoda, SOLA **6**, 17 (2010).
[16] D. J. Benney and A. C. Newell, J. Math. Phys. **46**, 133 (1967).
[17] M. J. Ablowitz and H. Segur, *Solitons and the Inverse Scattering Transform* (SIAM, Philadelphia, 1981).
[18] S. P. Novikov, S. V. Manakov, L. P. Pitaevskii, and V. E. Zakharov, *Theory of Solitons: The Inverse Scattering Method* (Plenum Press, New York, 1984).
[19] L. D. Fadeev and L. A. Takhtajan, *Hamiltonian Methods in the Theory of Solitons* (Springer-Verlag, Berlin, 1987).
[20] M. J. Ablowitz and P. A. Clarkson, *Solitons, Nonlinear Evolution Equations and Inverse Scattering* (Cambridge University Press, Cambridge, 1991).
[21] C. Sulem and P.-L. Sulem, *The Nonlinear Schrödinger Equation* (Springer-Verlag, New York, 1999).
[22] M. J. Ablowitz, B. Prinari, and A. D. Trubatch, *Discrete and Continuous Nonlinear Schrödinger Systems* (Cambridge University Press, Cambridge, 2004), Vol. 302.
[23] V. E. Zakharov and A. B. Shabat, Sov. Phys. JETP (Engl. Transl.) **34**, 62 (1972).
[24] M. B. Erdoğan and V. Zharnitsky, Commun. Math. Phys. **281**, 655 (2008).
[25] H. Hasimoto and H. Ono, J. Phys. Soc. Jpn. **33**, 805 (1972).
[26] J. Weideman and B. Herbst, SIAM J. Numer. Anal. **23**, 485 (1986).
[27] G. Agrawal, *Nonlinear Fiber Optics* (Academic Press, Waltham, MA, 2013).
[28] J. Satsuma and N. Yajima, Prog. Theor. Phys. Suppl. **55**, 284 (1974).
[29] W. H. Press, S. A. Teukolsky, W. T. Vetterling, and B. P. Flannery, *Numerical Recipes*, 3rd ed. (Cambridge University Press, Cambridge, 2007).
[30] T. R. Taha and M. I. Ablowitz, J. Comput. Phys. **55**, 203 (1984).
[31] B. Fornberg and G. B. Whitham, Philos. Trans. R. Soc. A Math. Phys. Eng. Sci. **289**, 373 (1979).
[32] U. M. Ascher and L. R. Petzold, *Computer Methods for Ordinary Differential Equations and Differential-Algebraic Equations* (SIAM, Philadelphia, 1998).
[33] R. Zwanzig, J. Chem. Phys. **33**, 1338 (1960).
[34] E. D. Belokolos, A. I. Bobenko, V. Z. Enol'skii, A. R. Its, and V. B. Matveev, *Algebro-geometric Approach to Nonlinear Integrable Equations*, Springer Series in Nonlinear Dynamics (Springer-Verlag, Berlin, 1994).
[35] M. U. Schmidt, *Integrable Systems and Riemann Surfaces of Infinite Genus*, Memoirs of the American Mathematical Society, Vol. 581 (American mathematical society, Providence, 1996).
[36] E. R. Tracy, H. H. Chen, and Y. C. Lee, Phys. Rev. Lett. **53**, 218 (1984).
[37] E. R. Tracy and H. H. Chen, Phys. Rev. A **37**, 815 (1988).
[38] N. Ercolani, M. Forest, and D. W. McLaughlin, Physica D **43**, 349 (1990).
[39] Y. Li and D. W. McLaughlin, Commun. Math. Phys. **162**, 175 (1994).
[40] G. D. Lyng and P. D. Miller, Commun Pure Appl. Math. **60**, 951 (2007).

[41] T. H. C. Herbers, S. Elgar, N. A. Sarap, and R. T. Guza, J. Phys. Oceanogr. **32**, 1181 (2002).
[42] E. Herbert, N. Mordant, and E. Falcon, Phys. Rev. Lett. **105**, 144502 (2010).
[43] K. L. Manktelow, M. J. Leamy, and M. Ruzzene, J. Vib. Acoust. **136**, 031016 (2014).
[44] K. Ohe, K. Asano, and S. Takeda, J. Phys. D **14**, 1023 (1981).
[45] X. Jiang, H. Yuan, and X. Sun, Sci. Rep. **6**, 39309 (2016).
[46] M. Onorato, A. R. Osborne, M. Serio, and L. Cavaleri, Phys. Fluids **17**, 078101 (2005).
[47] M. Onorato, A. Osborne, M. Serio, L. Cavaleri, C. Brandini, and C. Stansberg, Eur. J. Mech. B. Fluids **25**, 586 (2006).
[48] M. Onorato, S. Residori, U. Bortolozzo, A. Montina, and F. Arecchi, Phys. Rep. **528**, 47 (2013).
[49] A. Osborne, Fluids **4**, 72 (2019).
[50] G. Biondini and G. Kovačič, J. Math. Phys. **55**, 031506 (2014).
[51] R. Courant and F. John, *Introduction to Calculus and Analysis* (Springer-Verlag, New York, 1989), Vol. I.
[52] V. I. Arnold, in *Geometrical Methods in the Theory of Ordinary Differential Equations*, 2nd ed., edited by M. Levi, Grundlehren der mathematischen Wissenschaften (Springer Verlag, New York, 1988).
[53] F. Wang and A. K. Bajaj, J. Comput. Nonlin. Dyn. **4**, 021005 (2009).
[54] A. H. Nayfeh, *The Method of Normal Forms*, 2nd ed. (Wiley-VCH, Weinheim, 2011).
[55] S. Filip, A. Javeed, and L. Trefethen, SIAM Rev. **61**, 185 (2019).